

# Frictional melting of gabbro under extreme experimental conditions of normal stress, acceleration, and sliding velocity

André Niemeijer,<sup>1,2</sup> Giulio Di Toro,<sup>1,3</sup> Stefan Nielsen,<sup>1</sup> and Fabio Di Felice<sup>1</sup>

Received 24 December 2010; revised 14 April 2011; accepted 19 April 2011; published 16 July 2011.

[1] With the advent of high-velocity shear apparatus, several experimental studies have been performed in recent years, improving our understanding of the evolution of fault strength during seismic slip. However, these experiments were conducted under relatively low normal stress (<20 MPa) and using small cylindrical samples where a large gradient in slip velocity exists across the sliding surface. Given the above limitations, the extrapolation of these experimental results to natural conditions is not trivial. Here we present results from an experimental study on gabbroic rocks using a newly developed rotary shear apparatus capable of reaching higher normal stress (up to 50 MPa) on ring-shaped samples (30/50 mm internal/external diameter) and allowing precise control of the imposed slip velocity function. The results confirm that steady state shear stress during the melt-lubricated phase of the experiment depends on normal stress in the form of a power law equation as predicted by theoretical models. However, the exponent appears closer to 0.5, contrary to the theoretical prediction of 0.25. We observe no systematic dependence of shear stress on acceleration, but increasing deceleration drastically decreases the recovery of friction during final slip. We find that the slip-weakening distance decreases inversely with increasing normal stress, in agreement with theoretical considerations, and decreases with increasing slip rate. Extrapolation of the slip-weakening distance to natural conditions predicts a slip velocity for ancient seismic events of 0.3–1 m/s when compared with field estimates. These values compare well with seismological estimates.

**Citation:** Niemeijer, A., G. Di Toro, S. Nielsen, and F. Di Felice (2011), Frictional melting of gabbro under extreme experimental conditions of normal stress, acceleration, and sliding velocity, *J. Geophys. Res.*, 116, B07404, doi:10.1029/2010JB008181.

## 1. Introduction

[2] Because earthquakes generally nucleate at several kilometers of depth in Earth's crust, we can only investigate the physics of earthquakes through indirect means, using, for example, seismological observations or geodetic data (GPS, inSAR, etc.) collected at Earth's surface (for reviews, see Lee *et al.* [2002], Scholz [2002], and Abercrombie *et al.* [2006]). Although much can be learned about earthquake source parameters and physics using these methods (e.g., seismic waves analysis can be used to determine the seismic moment, the slip distribution, the radiated energy, the static stress drop and the rupture speed), fundamental information remains unknown [Kanamori and Heaton, 2000; Kanamori and Rivera, 2006]. Among these, the nature of the friction coefficient evolution during slip and its key role in the total energy budget of an earthquake are poorly resolved. Alternative

methods to study the physics of earthquakes consist of conducting (1) careful experimental studies measuring the strength of artificial (laboratory) faults and gouge-filled faults under controlled conditions of stress, temperature, slip velocity and displacement that reproduce seismic slip and (2) investigations on natural faults and fault rocks and the comparison with experimental products [e.g., Di Toro *et al.*, 2009].

[3] The emergence of rotary shear apparatuses has allowed researchers to reproduce the deformation of rocks under conditions approaching those encountered during earthquake slip, at least in terms of slip velocity (about 1 m/s) and slip (several meters for large magnitude earthquakes) but low normal stress (<20 MPa; see Spray [1987, 2005], Tsutsumi and Shimamoto [1997], Mizoguchi and Fukuyama [2010], Reches and Lockner [2010], and Di Toro *et al.* [2011] for reviews) or in terms of slip (several meters) and normal stress (up to 112 MPa) but low slip velocity (<5 mm/s) [e.g., Goldsby and Tullis, 2002]. In fact, an apparatus capable of simultaneously reproducing the full range of slip, slip rate, acceleration and normal stress conditions typical of earthquakes does not yet exist. In this study, we present results from experiments performed on gabbroic rock samples using a newly constructed high-velocity shear apparatus, which considerably extends the combination of normal stress, slip and slip velocities covered in previous studies and reproduces

<sup>1</sup>Istituto Nazionale di Geofisica e Vulcanologia, Rome, Italy.

<sup>2</sup>Now at Faculty of Geosciences, Utrecht University, Utrecht, Netherlands.

<sup>3</sup>Dipartimento di Geoscienze, Università degli Studi di Padova, Padua, Italy.

the conditions likely to occur in a natural earthquake in the shallow portion of the seismic crust.

[4] Faults cutting dry intrusive rocks (tonalite, gabbros, etc.) or high-grade metamorphic rocks (e.g., eclogitic, amphibolitic facies rocks) typically contain pseudotachylites [solidified frictional melts produced during rapid slip [Jeffreys, 1942; McKenzie and Brune, 1972; Sibson, 1975; Sibson and Toy, 2006; Andersen et al., 2008], especially when faults have been exhumed from seismogenic depths without having been altered or weathered. Experimental studies on the frictional properties of intrusive rocks at high sliding velocities have shown that rock melting occurs when a certain threshold combination of normal stress, sliding velocity and displacement is reached [Spray, 1987; Tsutsumi and Shimamoto, 1997]. Successive studies have shown that melting of fault rocks can lead to significant dynamic weakening of the artificial fault, provided that enough melt is produced to lubricate the entire fault surface [Hirose and Shimamoto, 2005a, 2005b; Spray, 2005; Del Gaudio et al., 2009]. Once a throughgoing melt layer is produced, the strength of the fault is determined by the viscosity of the melt and the strain rate in the melt [Hirose and Shimamoto, 2005a; Di Toro et al., 2006a]. Since the strain rate depends on the slip velocity and the thickness of the melt layer, the evolution of the latter is of paramount importance in controlling the strength. The melt production rate depends on the slip rate and normal stress (i.e., the power supplied to the sample) [see Nielsen et al., 2008] and contributes to thickening of the melt layer. However, this is counteracted by melt extrusion at the sample periphery. This condition is similar to that observed in nature where most of the friction melt produced in the slipping zone is injected in the wall rocks [e.g., Di Toro et al., 2005]. According to the theoretical interpretation by Nielsen et al. [2008], a balance is achieved between melt extrusion and melt production at the steady state, resulting in a constant thickness of the melt layer, though measuring this during experiments remains a technical challenge. Although these experimental and theoretical studies have demonstrated that melt lubrication can be an efficient weakening mechanism, details of the evolution of strength remain unsure, in particular owing to the relatively small range of normal stress and slip velocities that earlier machines could reach. These experiments were performed under relatively low normal stresses (<25 MPa) and without a good control on the acceleration and deceleration of the target slip velocity. Also, previous experiments were done on relatively small (usually  $\leq 25$  mm in diameter) solid cylindrical samples with a large gradient in slip velocity over the sample surface which may affect the quality of the frictional and shortening data, or at least render their extrapolation to natural conditions of frictional sliding during earthquakes extremely complex.

[5] As a consequence, theoretical models were proposed in order to extrapolate the behavior measured in experiments to conditions expected in earthquakes. For pervasive frictional melting, theoretical trends were obtained for both the steady state [Fialko and Khazan, 2005; Sirono et al., 2006; Nielsen et al., 2008] and the transient behavior [Nielsen et al., 2010a] which could only partly be verified by the available experimental data. Finally, the complexity of the initial phases of sliding preceding the pervasive melting and the severe weakening, have so far been hardly explored, either experi-

mentally or theoretically (see description on first/second peak in section 4).

[6] Here we present results from an experimental study using a newly constructed Slow to High Velocity Apparatus (SHIVA) installed at the Istituto Nazionale di Geofisica e Vulcanologia in Rome, designed to overcome most of the above experimental issues. The experimental results will be extrapolated to natural conditions and compared with earthquake source parameters estimated from pseudotachylite-bearing faults from the Outer Hebrides Thrust (Scotland).

## 2. SHIVA

[7] We show a schematic diagram of our newly designed experimental apparatus in Figure 1. The apparatus is 3.5 m in length, 1.7 m in height, 0.9 m in width, and consists of a solid concrete base weighing 4000 kg, aimed to reduce high-frequency (kHz) vibrations during the experiments. The rotary shaft is centered inside a ball-bearing housing (B in Figure 1a) and a pair of semirigid bellow couplings (G in Figure 1a) providing the necessary play to adjust minor misalignments of the shaft with respect to the rotational axis. The shaft is directly connected to a brushless motor with a maximum power output of 280 kW and a peak speed of 4000 rpm (K in Figure 1a). A second, smaller brushless motor with a maximum power output of 5.15 kW (J in Figure 1a) is connected to the rotary shaft through a gear box with a ratio 1:225 (H in Figure 1a) and a sprag clutch, which acts as a freewheel (I in Figure 1a). For further details on the small motor and the workings of the sprag clutch, see Di Toro et al. [2010]. The motors can be controlled either in torque or in velocity (displacement) mode through an inverter/controller (not shown in Figure 1) which produces highly harmonic triphase currents, which can be modulated both in power and frequency. The inverter/controller is servoregulated through a feedback loop, using the position monitored within the motor with an optical encoder. The combination of current frequency (regulating the velocity) and electric power (regulating the torque required to rotate the shaft) determine the behavior of the motor. All parameters are updated inside the inverter/controller at a frequency of 16 kHz. Rotational displacement was also measured directly behind the ball-bearing housing; that is,  $\sim 30$  cm behind the sample sliding surface (Figure 1b). Initially, a commercial high-resolution optical encoder was installed with a resolution of  $0.2 \mu\text{m}$ . However, since this encoder has 629,760 counts per rotation, it was not possible to measure motor speeds above  $\sim 60$  rpm owing to the excessive frequency of the counts. Therefore, a second lower-resolution optical encoder was designed in house with 400 counts per rotation or a resolution of  $\sim 400 \mu\text{m}$ . In most of the experiments reported here (up to experiment number s074) the newly designed, external encoder was not yet installed on the shaft. For those experiments, motor speeds above 60 rpm were measured with the optical encoder installed within the large motor instead.

[8] Normal force was applied to the sample via an air-actuated intensifier (C in Figure 1a), acting through an arm (F in Figure 1a) to amplify the resulting normal force, allowing to reach a maximum force of 50 kN. Normal load was measured with a 50 kN load cell (50 N resolution) located behind a second ball-bearing housing that holds the nonrotating shaft

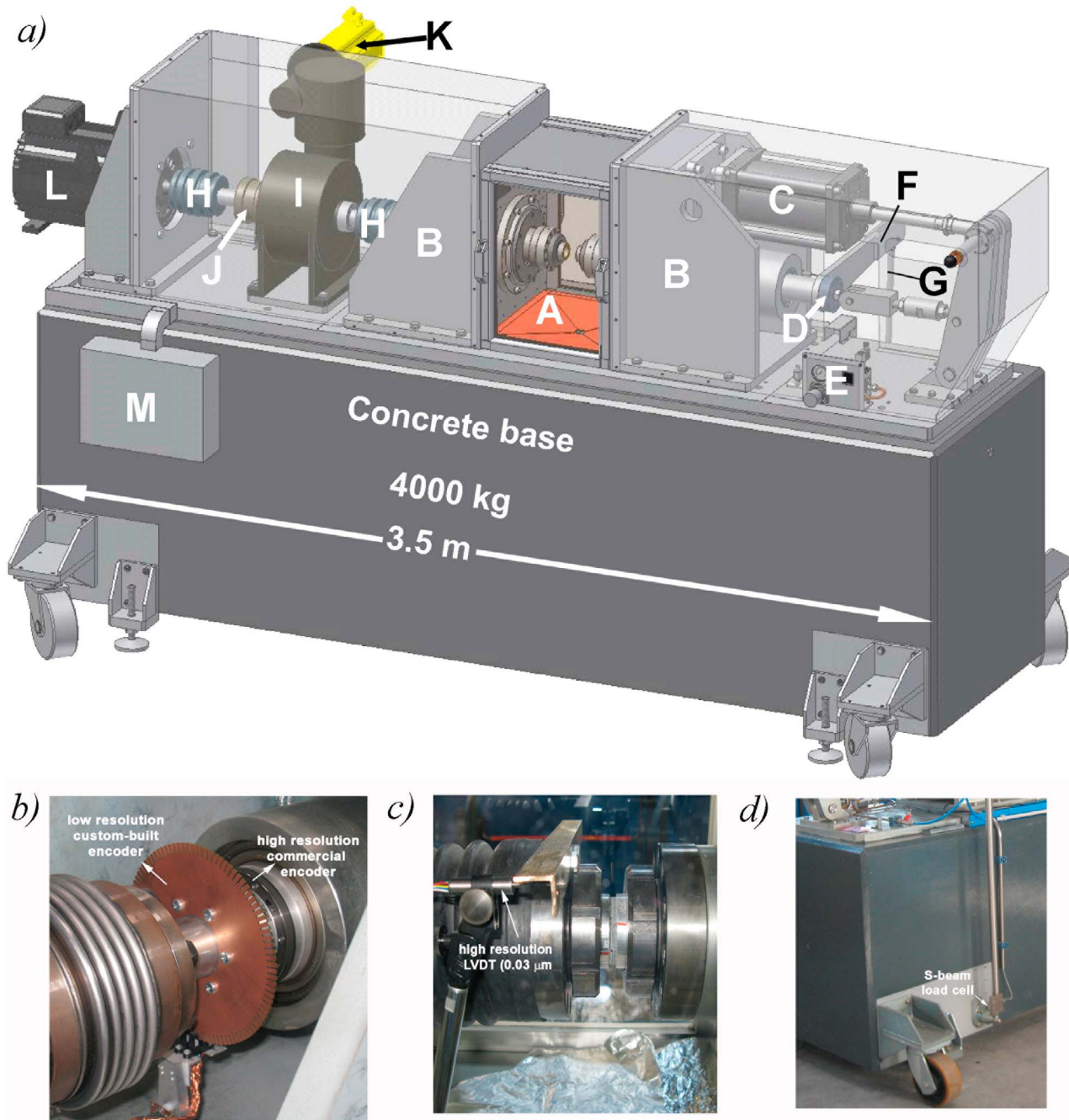


**Figure 1.** The Slow to High Velocity Apparatus (SHIVA). (a) Diagram showing the experimental apparatus: A, sample chamber; B, ball bearing housings; C, air actuator; D, axial load cell; E, computer-controlled air pressure valve; F, steel arm; G, torque bar; H, bellow couplings; I, gear box (1:225); J, sprag clutch; K, small engine; L, large engine; and M, data acquisition hardware. (b) Photograph of the two optical encoders used to measured rotational displacement. (c) Photograph of the high-resolution LVDT showing its position relative to the sample sliding surface. (d) Photograph showing the location of the S-beam load cell used in extension to measure the torque.

(D in Figure 1a). Displacement of the nonrotating shaft in the horizontal direction was measured with a 50 mm full-scale direct current linear variable differential transformer (DCDT,  $\sim 50 \mu\text{m}$  resolution), mounted behind the ball bearing housing, and with a 3 mm full-scale linear variable differential

transformer (LVDT;  $\sim 0.03 \mu\text{m}$  resolution) mounted inside the sample chamber close to the sample sliding surface (Figure 1c). The nonrotating shaft is prevented from rotating by a 50 cm long arm (F in Figure 1a) attached to the concrete base through a vertical steel bar. Torque was measured via a

**Table 1.** Composition of the Rock (Microgabbro) Used in the Experiments as Determined by Rietveld XRD Analysis and the Thermal Properties of Its Minerals<sup>a</sup>

Mineral	wt %	$T_{\text{melt}}$ (K)	$C_p$ at 1100 K ( $\text{J kg}^{-1}\text{K}^{-1}$ )	$\rho$ ( $\text{kg m}^{-3}$ )	$\Delta H$ ( $\text{kJ kg}^{-1}$ )	$\tau_a$ (GPa)	$C_p$ at 300 K ( $\text{J kg}^{-1}\text{K}^{-1}$ )
Labradorite (Pl)	35.5	1800	1167	2765	302	7.62	763
Enstatite (Opx)	6.8	1700	1282	3204	373	6.91	824
Diopsid (Cpx)	39.6	1670	1164	3279	372	6.24	775
Quartz (Qtz)	7.4	2000	1197	2650	302	10.87	756
Biotite (Bt)	4.4	930	1079	3215	453	0.8 <sup>b</sup>	732
Hornblende (Hbl)	5.2	1273	1204	3165	380	6.24	759
Magnetite (Mag)	0.7	1811	913	5150	597	~7	654
Total (microgabbro)	99.6		1167	3037	344		

<sup>a</sup> $T_{\text{melt}}$  is the melting temperature,  $C_p$  is the specific heat capacity at constant pressure,  $\rho$  is the density,  $\Delta H$  is the latent heat of fusion, and  $\tau_a$  is the local shear strength (taken as the indentation hardness; see Beeler *et al.* [2008]).

<sup>b</sup>Data for muscovite.

S-beam type load cell (operating in extension, 3 kN full scale and 3 N resolution) located between the vertical bar and the horizontal arm (Figure 1d).

[9] Data were acquired from all available sensors by a National Instruments Compactrio using a 24 bit 250 mV full-scale strain module for the load cells, a 16 bit, 10 V full-scale analog input module for the horizontal displacement sensors and a digital input module for the two encoders. A field programmable gate array (FPGA) was programmed using a compiled Labview virtual instrument (VI) to acquire the signals from these modules at a rate of 25 kHz to prevent latencies and real-time dataflow problems. In addition, air pressure can be controlled through the FPGA. Data were monitored and preprocessed in real time using a Labview VI (virtual instrument), typically at a recording rate of 25 kHz during the high-speed section of the experiments. During most experiments, we recorded the speed of the motors through the software of the inverter/controller. Owing to the small memory available in the inverter/controller, the recording rate here was 1 kHz. The data from Labview were therefore decimated down to 1 kHz to allow for synchronization of the two data sets and to reduce the number of data points. However, analysis of peak and steady state friction was done on the raw 25 kHz data set. Some of the experiments reported here were monitored with a high-speed camera (acquisition rate of 10 frames per ms) to better interpret the mechanical data.

### 3. Experimental Procedure

[10] We used samples of quartz microgabbro (commercial name “Absolute black”), purchased from a rock seller in Rome and quarried from the Bushveld igneous complex, South Africa. Mineralogical compositions were determined by quantitative XRD analysis (Rietveld method) on powders of the sample (Table 1). The main minerals are plagioclase, clinopyroxene, orthopyroxene, quartz and minor amphibole and biotite. The grain size is in the range 0.5–1 mm. Samples were cut from ~40 mm thick slabs by a hydrocut water jet procedure, which produced rings of ~30 mm inside diameter and 50 mm outside diameter. The rings were clamped inside precut aluminum rings with an inside diameter of 50 mm and an outside diameter of 55 mm (Figure 2). The aluminum rings were introduced in order to distribute the clamping pressure on the rock sample and, in some cases, to cover and sustain portions of the sample emerging from the holder. In some cases, aluminum foil was used to increase the diameter of the

samples to provide a tight fit and in other cases the periphery of the samples was ground using sanding paper. The sample plus aluminum ring was then placed inside a stainless steel pincer, which was subsequently placed in the sample holders in the machine (Figure 2). A locking ring was screwed and tightened over the pincer plus sample, effectively clamping the sample and aluminum ring assembly.

[11] Owing to the irregular nature of the cuts by the hydrocut (e.g., the faces might not be perfectly orthogonal to the walls of the cylinder), the sample surfaces were in all cases misaligned to varying degrees. Therefore, samples were preground at a speed of 10 to 20 rpm (or an equivalent slip velocity of 2 to 4 cm/s) with a normal load of  $\leq 0.5$  MPa. During grinding, the samples were regularly cleaned with a medium-hardness toothbrush and pressurized air. We show the evolution of the friction coefficient (equal to shear stress/normal stress) and shortening with displacement in Figure 3. Both the friction coefficient and shortening vary greatly initially with a period that is equal to one rotation (see zoomed plots), but the amplitude of the oscillations decreases substantially with increasing displacement. The oscillations are clearly the result of misalignment of the rock faces, which leads to fluctuations in the area of the sample that is in contact

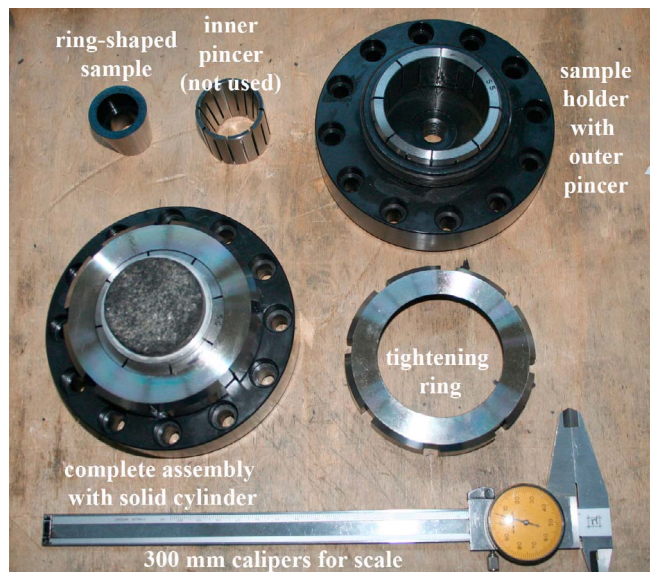


**Figure 2.** Photograph of the sample assembly showing the rings of gabbro, aluminum rings, and metal clamping ring.

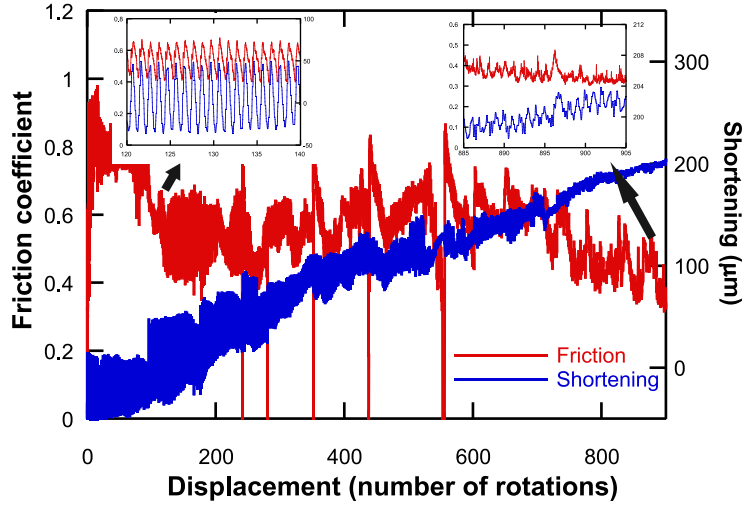


**Figure 3.** Plot showing the friction coefficient and sample shortening versus displacement during the initial grinding procedure. The two insets show details of the initial and final parts. In all experiments, grinding was continued until the amplitude of the oscillations in shortening was smaller than  $5 \mu\text{m}$ . For further details, see main text.

and, more importantly, to a noncoaxial alignment of the area of contact. The grinding away of the sample surface reduces the misalignment, ultimately reducing the amplitude of the oscillations in shortening to below  $\sim 2 \mu\text{m}$  and in friction coefficient to less than  $\sim 0.1$  (note that the normal stress was very low during grinding, so that the resolution in friction coefficient is not very high). The sample pair was deemed parallel and thus ready for the actual experiment when the amplitude of the oscillations of the LVDT (axial shortening) was lower than  $3 \mu\text{m}$  and/or the sample was fully covered with powdered gouge material (Figure 4). At this point, both surfaces were thoroughly cleaned with the toothbrush and pressurized air to remove all wear material.

[12] For the actual experiment, the sample was loaded incrementally to the desired load and kept at this load for 5–15 min. Then, the prescribed velocity function was applied by switching on the motor, while acquiring data at the maximum rate of 25 kHz. In all the experiments, we imposed at least 49 rotations to the samples (equivalent to a total slip of 6 m, see below). When the velocity function was finished, we lowered the recording rate, disabled the motor and removed the normal load. Before moving back the axial column, we applied cyanoacrylate glue to the surface of the (now welded) sample pair and removed the tightening ring on the stationary side. In this manner, we were able to recover the sample pairs in one piece from the rotary side in 90% of the cases. Successfully recovered sample pairs were then impregnated with epoxy resin and thin sections for optical and electron microscopy observations were cut across the rings tangential (subparallel) to the sliding direction.

#### 4. Results

[13] In the following, we present a summary of the experimental data obtained in this study. All experiments and their corresponding conditions are listed in Table 2. The friction coefficient ( $\mu$  or ratio of shear stress  $\tau$  and normal stress  $\sigma_n$ ), displacement and sliding velocity vary from the outer to the

inner rim of the samples: we calculate an equivalent slip velocity, displacement and shear stress, from the acquired raw data (measured torque, normal load, angular speed) using the equations described in the work of Shimamoto and Tsutsumi [1994], Hirose and Shimamoto [2005a], and Di Toro *et al.* [2010].

#### 4.1. Shear Stress and Shortening

[14] We show the evolution of shear stress, normal stress, friction coefficient, shortening and slip velocity as a function of both time and slip for a typical experiment conducted at 20 MPa normal stress, 3 m/s sliding velocity and an acceleration and deceleration of  $30 \text{ m/s}^2$  in Figure 5. Unless otherwise specified, the deceleration was the same as the acceleration in all experiments (see also Table 2).

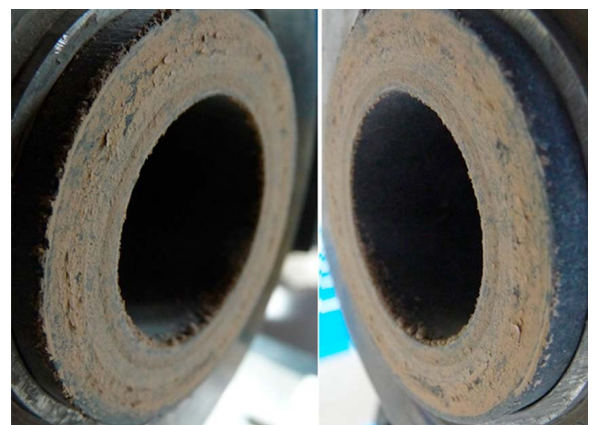


**Figure 4.** Photograph of the two sides of a gabbro sample at the end of the grinding procedure. Note that both surfaces are fully covered with a reddish-brown gouge. These surfaces were cleaned with a medium-hardness toothbrush and compressed air before the high-speed experiment.

**Table 2.** List of Experiments and Conditions

Experiment	$\sigma_n$ (MPa)	V (m/s)	a (m/s <sup>2</sup> )	d (m)	$\mu_{ss}$	Notes
s042	40	6.5	65	14.93	0.052	
s049	20	3	30	6	0.110	
s050	20	3	30	6	0.105	
s051	20	3	6	6	0.106	
s052	20	3	3	6	0.120	
s053	20	3	3	6	0.105	
s054	20	3	6	6	0.111	
s056	20	3	15	6	0.112	
s058	20	3	15	7.81	0.101	
s059	20	3	15	6	0.103	
s062	40	3	30	6	0.075	
s063	40	3	3	6	0.073	
s064	10	3	30	6	0.147	
s065	10	3	3	6	0.175	
s066	20	5	30	6	0.103	
s067	20	6.5	30	6	0.109	
s070	20	1	30	~4	0.112	reached end of axial stroke
s071	15.5	1.14	2.85	15.21	0.145	
s072	1.4	$10^{-3}$ –0.8	5	68.20	0.662	
s073	5	$10^{-3}$ –3	30	6	0.258	
s074	10	3	30	6	0.145	
s079	15	3	30	6	0.126	
s082	20	3	60	6	0.106	
s088	20	3	2	6	0.105	
s097	30	3	30	6	0.089	
s106	5	3	30	6	0.265	
s107	30	3	3	6	0.092	
s111	2.5	3	30	14.56	0.358	
s113	7.5	3	30	9.14	0.195	
s114	50	3	30	0.45	0.071	40/50; sample failed
s115	1	3	30	22.08	0.556	
s117	0.7	3–0.3	30	35.43	0.494	
s129	10	1.3	3.25	10.08	0.098	solid 50 mm

[15] Normal stress initially decreases by up to 5% (note the change in scale in the normal stress axis), indicating that the air-actuated system is not able to keep up with the fast shortening of the sample (either because the response time of the electrovalve that controls the pressure is too long or because the friction of the seal inside the actuator prevents fast movement). However, the drop in normal stress is relatively small and we use the measured instantaneous normal stress in all our calculations of the friction coefficient, so it does not affect the results. Also, we can see in Figure 5b that the imposed slip velocity displays a small overshoot (less than 5%) in the acceleration. Since we are mostly interested in the steady state portion of the experiment in this contribution, we do not consider these to be of importance (and the overshoots are very short-lived in comparison to the duration of the experiment).

[16] Shear stress increases abruptly upon initial sliding, reaching a first peak (after ~10 ms in the specific case of experiment s049; see point a in Figure 5a), followed by an abrupt drop (point b) and then a more gradual increase reaching a broad maximum/peak (point c), after which shear stress decays (transient stage) toward a steady state value after ~500 ms (~1 m of slip; see point d). Note that the timing of the peaks described in the example of Figure 5a are not general but strongly depend on the experimental conditions applied. Shear stress remains constant during the remainder of the experiment until the sliding velocity decreases and shear stress increases (point e), reaching a maximum at the end of the experiment (point f). This sequence of first weakening (points a to b), strengthening (points b to c) and second

weakening (points c to d) toward steady state shear stress is similar to the one described in similar rocks (India gabbro) by *Tsutsumi and Shimamoto [1997]* and *Hirose and Shimamoto [2005a]*. The measured axial displacement is virtually zero during the initial part of the experiment, but when the shear stress decays after the (second) broad maximum, the sample shortens at a roughly constant rate, consistent with observation of full-scale melt production and extrusion. Note that Figure 5 displays one out of every 25 data points (i.e., decimated data) to facilitate synchronization with the data acquired from the motor (which was recorded at 1 kHz) but the data are not filtered. As a result, we can observe oscillations in the shear stress and shortening. Though very stiff compared to other rotary shear apparatuses (the measured stiffness is 1.63 Nm/ $\mu\text{m}$  in rotation and 0.22 kN/ $\mu\text{m}$  in the axial direction), SHIVA is not infinitely stiff and vibrates when excited under the extreme deformation conditions imposed in the experiments. Vibrations are induced by (1) the energy input from the motor (in some experiments, the sample accelerates from 0 to 3000 rpm in 0.1 s, which is almost like hammering the sample) and (2) slight sample misalignment. The vibrations with the largest amplitude occur at a frequency of about 200 Hz. Detailed analysis of the typical frequencies of SHIVA by means of (1) FEM modeling and (2) accelerometers located in several parts of the apparatus have shown that 200 Hz is the characteristic frequency of the apparatus and especially of the stationary loading column and the torque bar. Therefore, in the following we show data that have been averaged over 250 records (similar to applying a filter at a frequency of 100 Hz) to reduce the

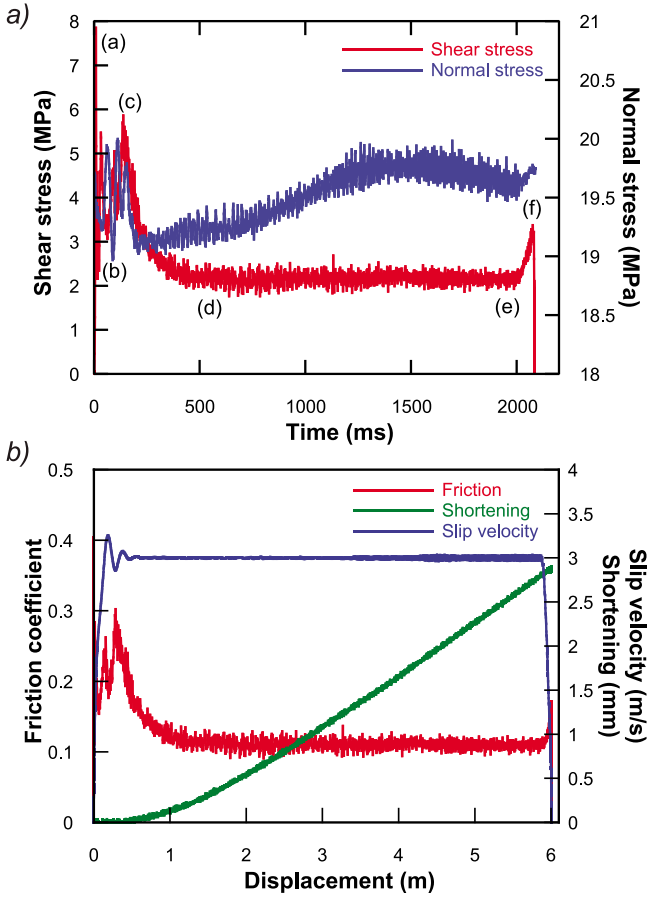


**Figure 5.** (a) Plot showing the evolution of shear and normal stress with time during a typical experiment (s049). Points a–f are explained in the main text. (b) Plot showing the evolution of the friction coefficient, slip velocity, and shortening with displacement of the same experiment (s049).

effects of vibrations on the measured shear stress and friction and then decimated to 1 kHz to allow for synchronization with the data from the motor encoder and to reduce the number of data to be plotted.

#### 4.2. Effect of Normal Stress on Friction Coefficient and Shortening

[17] In Figure 6a we show the evolution of friction coefficient with displacement for experiments performed at 5, 20 and 40 MPa normal stress with a sliding velocity of 3 m/s and an acceleration of 30 m/s<sup>2</sup>. It is obvious that normal stress has a large effect on both the initial evolution of the coefficient of friction and the level of the friction coefficient at steady state. The latter dependence is typical of melt lubrication [Persson, 2000; Di Toro *et al.*, 2006b]; in fact, in solid friction, the friction coefficient is almost independent of the applied normal stress [e.g., Byerlee, 1978]. We will discuss the initial evolution of friction coefficient in a future contribution and focus here on the steady state friction coefficient. Steady state friction is reached within the first meter of slip when normal stress is high (40 MPa). With decreasing normal stress, the amount of displacement needed to reach steady state friction increases, as does the coefficient of friction. In fact, the experiments performed at normal stresses lower than 5 MPa

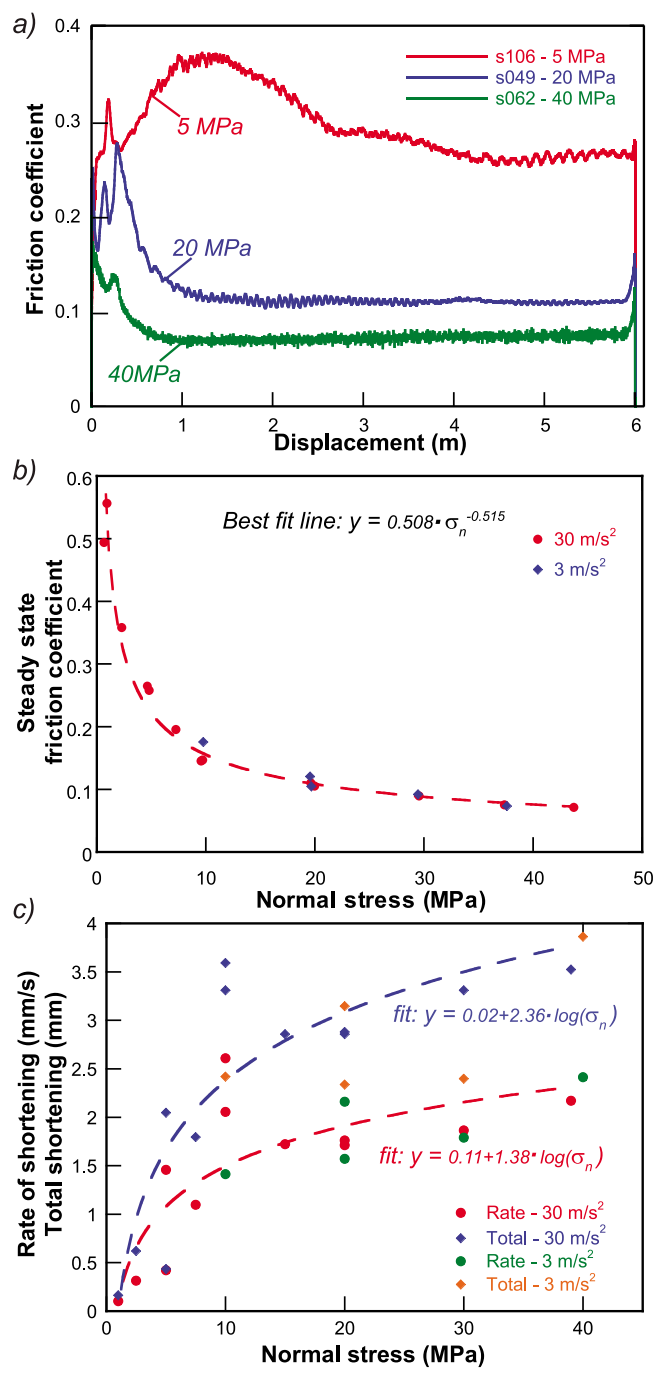


**Figure 6.** Plots of friction and shortening for experiments with varying normal stress. Slip velocity is 3 m/s, and acceleration is deceleration is 30 m/s<sup>2</sup> in all cases unless indicated otherwise. (a) Plot showing the evolution of friction with displacement for three experiments with different normal stresses (s049, s062, and s106; see also Table 2). Note that the data were averaged over 250 records (reducing the number of data to 1 point per 0.01 s). (b) Plot showing steady state friction as a function of normal stress for all experiments with variable normal stress (see Table 2). Note that duplicate experiments were performed at 20 MPa. Also shown is a best fit line through all data. (c) Plot showing the average rate of shortening and the total amount of shortening as a function of normal stress for the same experiments as in Figure 6b.

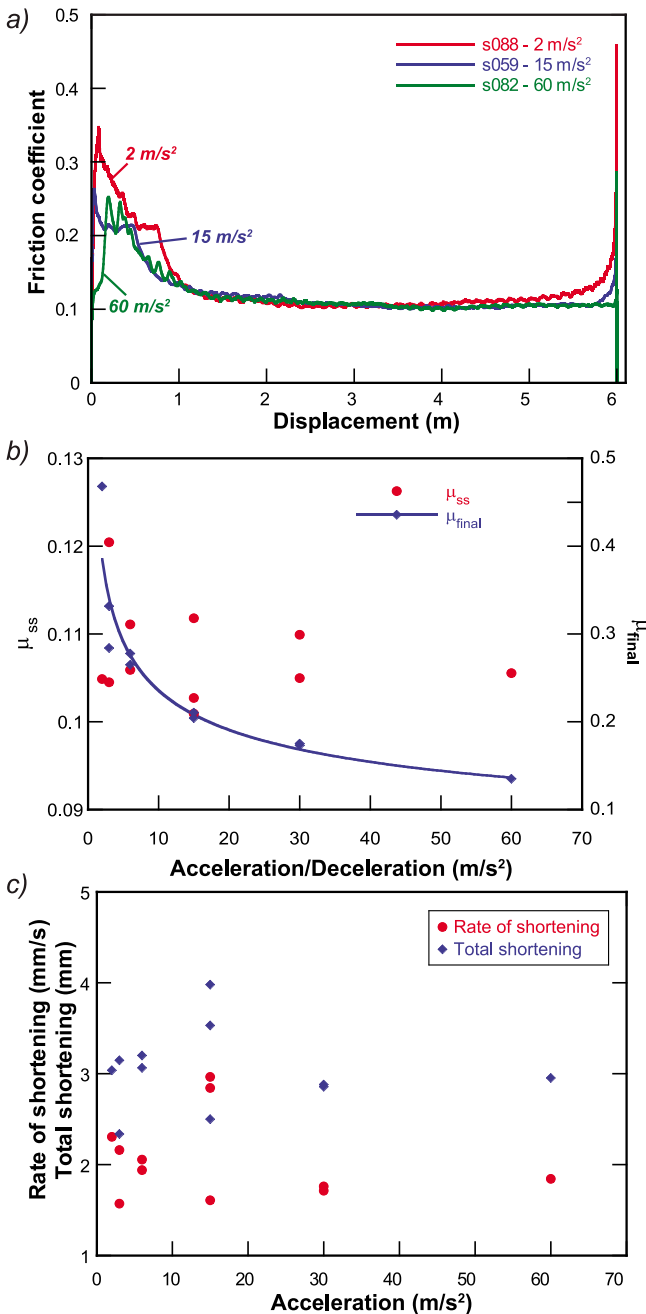


**Figure 7.** Plots of friction and shortening for experiments with varying accelerations/decelerations. Slip velocity is 3 m/s, and normal stress is 20 MPa in all cases. (a) Plot showing the evolution of friction with displacement for three experiments with different accelerations (s059, s082, and s088; see also Table 2). Note that the data were averaged over 250 records (reducing the number of data to 1 point per 0.01 s). (b) Plot showing steady state and final friction as a function of acceleration. Also shown is a best fit line through the final friction data. Note that the vertical scale of the steady state friction covers only 0.04 units in friction. (c) Plot showing the average rate of shortening and the total amount of shortening as a function of acceleration.

required more than the 6 m of displacement typically imposed to reach steady state. In Figure 6b, we plot the steady state friction coefficient as a function of normal stress. Steady state friction coefficient values were determined by averaging over a period of 0.2 s (or 0.6 m of displacement and 5000 records) before the onset of restrengthening (i.e., at a displacement of  $\sim 5.5$  m for 30 m/s<sup>2</sup> deceleration at high normal stress). We observe a strong dependence of the steady state friction coefficient on normal stress, defining a best fit curve with a power law equation of the form

$$y = A \cdot x^B \quad (1)$$

with in this case A taking the value of 0.51 and B is  $-0.52$ , with a  $R^2$  value of 0.945.

[18] In Figure 6b, we also show the steady state data from five experiments that were performed with a different velocity profile; that is, with an acceleration/deceleration of 3 m/s<sup>2</sup>. These data follow the general trend defined by the data from the experiments performed with an acceleration of 30 m/s<sup>2</sup>. When we look at the shortening data, we observe a general increase in the total amount of shortening and of the shortening rate at steady state with increasing normal stress (Figure 6c). Although there is considerable scatter, we can tentatively fit the data with a curve of the type

$$y = A + B \log(\sigma_n) \quad (2)$$

where A is 0.11 and 0.02 and B is 1.38 and 2.36 for the rate of shortening at steady state and the total shortening, respectively. Again, we also report data from the experiments with slower acceleration and these generally follow the trend defined by the 30 m/s<sup>2</sup> data.

#### 4.3. Effect of Acceleration and Deceleration on Friction Coefficient and Shortening

[19] We systematically varied the acceleration and deceleration to investigate their effects on initial friction coefficient evolution (points a–c in Figure 5a), steady state friction coefficient (points d and e in Figure 5a) and final friction coefficient (points e and f in Figure 5a: restrengthening). Again, here we focus on the steady state and final part of the experiment. We note that in most cases the target slip velocity was reached before the occurrence of the second broad peak. We show the results of three such experiments in Figure 7a and summarize all steady state results as a function of acceleration in Figure 7b. It is clear that there is no discernible effect of the initial acceleration on the steady state friction coefficient (note that the scale in Figure 7b is 0.04 in nondimensional friction units), but we do observe an obvious increase in the final friction coefficient with decreasing deceleration. Equation (1) can be used to fit these data with A is 0.476 and B is  $-0.305$ . We do not observe any obvious dependence of the shortening rate or total amount of shortening as a function of acceleration (Figure 7c).

#### 4.4. Effect of Slip Velocity on Friction Coefficient and Shortening

[20] The results of all experiments performed with different sliding velocity, but otherwise the same conditions (20 MPa normal stress, 30 m/s<sup>2</sup> acceleration), are shown in Figure 8. We observe a similar evolution of friction coefficient for all

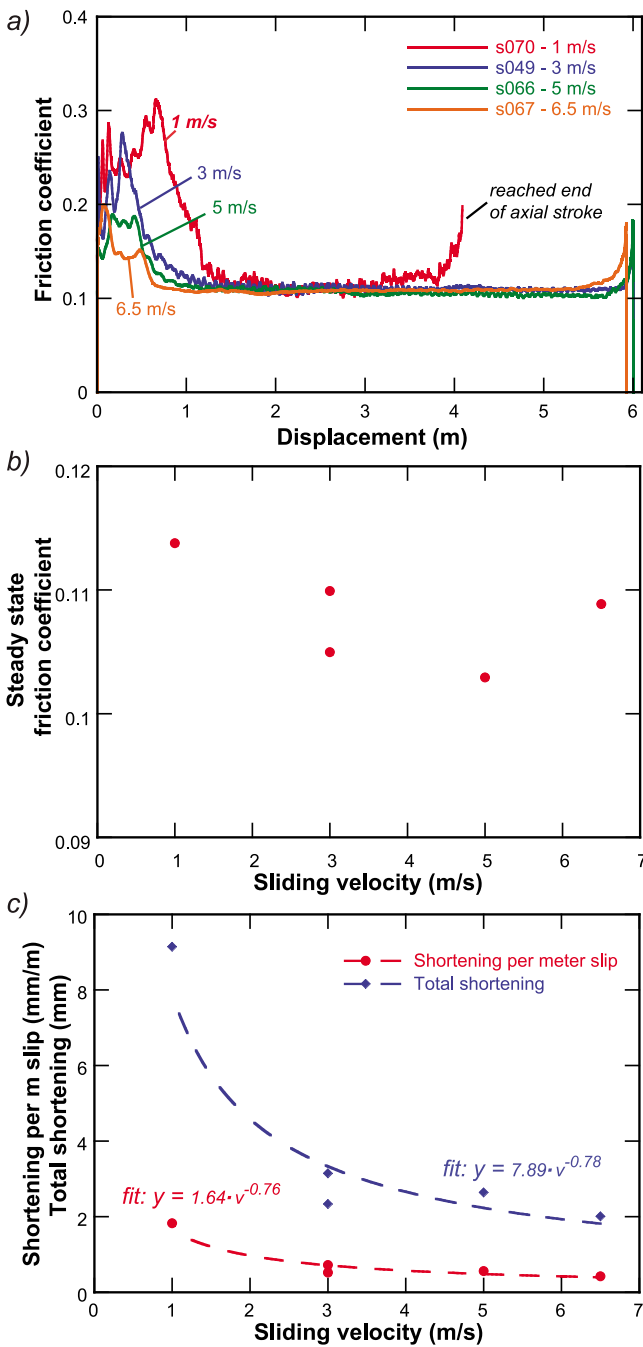


**Figure 8.** Plots of friction and shortening for experiments with varying peak slip velocities. Acceleration is deceleration is  $30 \text{ m/s}^2$ , and normal stress is 20 MPa in all cases. (a) Plot showing the evolution of friction with displacement for four experiments with different slip velocities (s049, s066, s067, and s070; see Table 1). Note that the data were averaged over 250 records (reducing the number of data to 1 point per 0.01 s). Also note that experiment s070 was ended prematurely because the axial column reached its end position, leading to a reduction in normal stress. (b) Plot showing steady state friction as a function of slip velocity. (c) Plot showing the average shortening per meter of slip (in mm/m) and the total amount of shortening as a function of slip velocity.

sliding velocities. Steady state is reached at smaller displacements with increasing sliding velocity. However, the steady state friction coefficient does not vary significantly with sliding velocity (Figure 8b), though a tendency for a lower friction coefficient with increasing velocity might be implied. In contrast, both the shortening per meter of slip (mm/m) and the total amount of shortening (the total slip was 6 m for all but s070, for which we extrapolate the shortening to 6 m slip) show a strong decrease with increasing sliding velocity (Figure 8c). A best fit curve describing the data can be drawn using equation (1) where A is 1.64 and 7.89 and B is  $-0.76$  and  $-0.78$  for the rate of shortening and total shortening, respectively.

#### 4.5. Comparison With Results From the Rotary Shear HV-1 in Kochi, Japan

[21] We compared the results of one experiment performed on identical samples of gabbro using the HV-1 rotary shear apparatus designed by T. Shimamoto and now installed in Kochi (Japan) with the results obtained from SHIVA (Figure 9). The HV-1 is probably the most exploited high-velocity friction apparatus in the geophysical literature, as, starting from 1994, it performed more than 2000 experiments on different types of cohesive (silica-, calcite-, and gypsum-built rocks) and noncohesive (clay-rich, gypsum, dolomite, lime, etc., bearing powders) rocks (for a description of HV-1, see, e.g., Shimamoto and Tsutsumi [1994] and Hirose and Shimamoto, 2005a; for a review of the mechanical data, see Di Toro *et al.* [2011]). The HV-1 has several limitations compared to SHIVA in terms of available power (11 kW versus 280 kW), normal load (1 ton versus 5 tons), angular speed (1500 rpm versus 4000 rpm) and sample size (usually 25 mm versus 50 mm exterior diameter). In fact, the HV-1 can perform experiments also with 40 mm in diameter samples, but the limited normal load and power available impedes the application of larger normal stresses. In the comparison between the two instruments, we used solid cylinders 25 and 50 mm in diameter in the HV-1 and SHIVA, respectively. Note that to reproduce the same acceleration and normal stress, the sample size used in the HV-1 was 25 mm and not the maximum possible size of 40 mm. We imposed the same velocity function (acceleration from 0 to an equivalent slip rate of 1.3 m/s in 400 ms, constant slip rate of 1.3 m/s for 10 m of slip and deceleration in 500 ms) and same normal stress of 10 MPa to the samples. The results from the two experiments are shown in Figure 9. At first glance, the results appear very different, but they are actually quite similar.

[22] First of all, the initial first peak in friction coefficient is comparable in terms of level (0.42); however, the friction drops much faster in the experiment performed using SHIVA, which might be explained by the much higher machine stiffness. After this first weakening phase, both experiments show a steady increase in friction until a second broad peak is reached. Again, the level of friction and the displacement at which the broad peak occurs is very similar. After the second peak, the measured friction of the two experiments starts to diverge significantly and the steady state value in the experiment performed with SHIVA is much lower than that obtained with HV-1. This can be explained by the different sample sizes used. Because the experiment with SHIVA uses a solid 50 mm sample, the melt extrusion rate is much lower than in the experiment with HV-1 that uses a 25 mm diameter

sample. The larger average flow distance of melt before extrusion in the experiments performed with SHIVA, slows down melt extrusion. This results in a thicker melt layer, a weaker resistance to shear and thus a more efficient lubrication of the experimental fault. Nielsen *et al.* [2008] already predicted the role of sample size using their theoretical model for melt lubrication which includes the melt extrusion problem. In fact, using their model, we can predict a strength contrast at steady state for the two samples sizes of roughly  $1/\sqrt{2}$  which is close to the measured difference (Figure 9). For the same reason, we expect a higher shortening rate for the experiment performed with the smaller sample, which is what we observe. The only major discrepancy is in the restrengthening in the final slip stages, which is much higher in the HV-1 experiment. However, the HV-1 is not capable of braking instantaneously or in a controlled fashion as SHIVA and thus there was probably a more gradual decrease in rotation rate toward the end of the experiment (T. Hirose, personal communication, 2010), allowing time for an increased restrengthening. All in all, we can conclude that the comparison of the two instruments is very favorable.

## 5. Microstructural Observations

[23] In Figure 10, we show scanning electron microscope (SEM) images of two experiments, s062 and s064, showing a throughgoing quenched melt layer. The thickness and roughness of the boundary between the quenched melt and the wall rock is highly variable along the length of the slip zone, with the thickness varying from  $\sim 1 \mu\text{m}$  up to several hundreds of micrometers. The quenched melt contains numerous suspended clasts of wall rock fragments, corresponding to about 30% of the total volume. In addition,

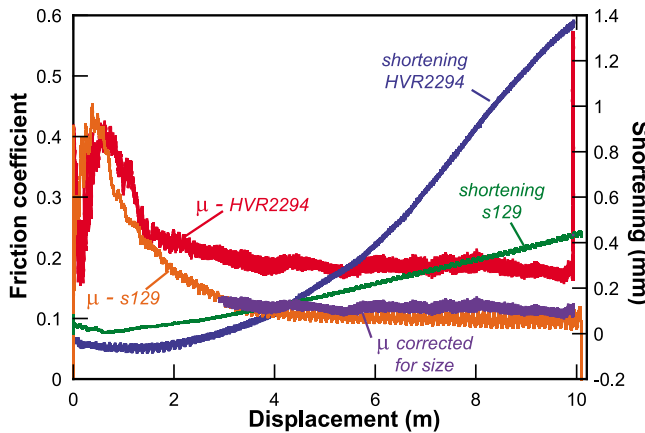


**Figure 9.** Comparison of the evolution of friction and sample shortening as a function of displacement for a 24.96 mm solid cylindrical sample of (identical) gabbro deformed using HV-1 in Kochi, Japan (HVR2294), and a 50 mm sample of gabbro deformed using SHIVA in Rome, Italy (s129), under otherwise identical conditions (normal stress of 10 MPa, slip velocity of 1.3 m/s, and acceleration of  $\sim 3.25 \text{ m/s}^2$ ). The purple curve shows the steady state shear stress of HVR2294 recalculated for a sample of 50 mm in diameter (same size as the sample run with SHIVA). See discussion in the main text.

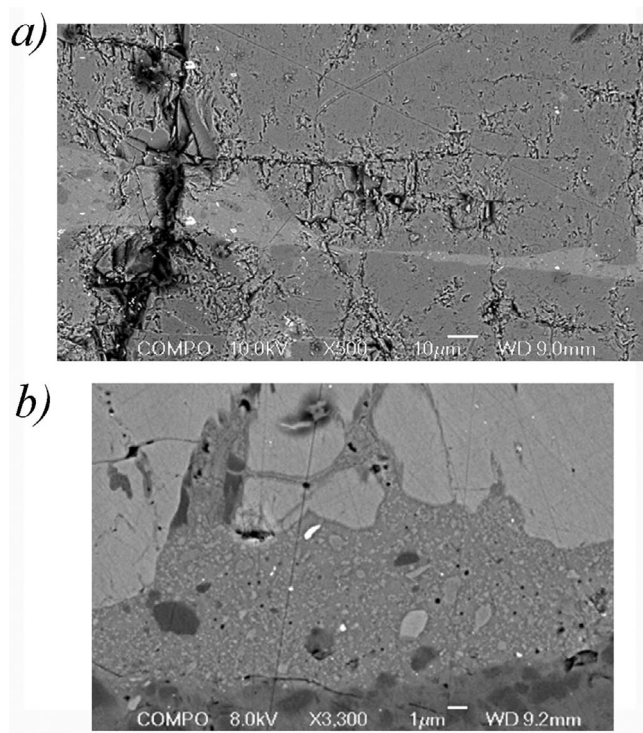


**Figure 10.** (a) Scanning electron microscope backscattered electron (SEM-BSE) image of sample s064 (normal stress of 10 MPa, slip velocity of 3 m/s, and acceleration of  $30 \text{ m/s}^2$ ) showing a throughgoing layer of quenched melt with varying thickness and numerous clasts. (b) SEM-BSE image of sample s062 (normal stress of 40 MPa, slip velocity of 3 m/s, and acceleration of  $30 \text{ m/s}^2$ ) showing numerous clasts (corresponding to about 30% in volume) embedded in the quenched melt injected into the wall rock.

in some locations we can observe the quenched melt fingering into the wall rock (Figure 10b), not unlike injection veins commonly found in exhumed pseudotachylite-bearing fault rocks. A detailed quantitative analysis of the melt composition, roughness and thickness (variation) is beyond the scope of this manuscript, but will be the focus of a future contribution.

## 6. Discussion

### 6.1. Evolution of Friction Coefficient

[24] Our experimental results are very similar to results from previous experimental studies on frictional melting at fast slip rates in cohesive rocks [e.g., Tsutsumi and Shimamoto, 1997; Hirose and Shimamoto, 2005a, 2005b; Del Gaudio *et al.*, 2009]. Moreover, the direct comparison between the experimental data obtained with SHIVA and HV-1 using the same rock type shows that the data we obtained are robust and reproducible (section 4.5). Shear stress increases sharply to a first peak (point a in Figure 5a) and then drops over a short time interval, the duration of which seems to increase with decreasing acceleration. This, and evidence from earlier studies, suggests that the initial peak and subsequent weakening is caused by flash weaken-

ing; that is, the heating and thermal weakening of initially small asperity contacts. Theoretical models for flash weakening predict a threshold slip velocity that is given by:

$$v_w = \frac{\pi\alpha}{D_a} \left( \frac{\rho C_p (T_w - T)}{\tau_a} \right) \quad (3)$$

[Rice, 1999, 2006] where  $\alpha$  is the thermal diffusivity,  $D_a$  is the asperity size,  $\rho$  is the rock density,  $C_p$  is the specific heat capacity at constant pressure,  $T_w$  is the temperature above which weakening occurs,  $T$  is the temperature and  $\tau_a$  is the local shear strength of the asperity [e.g., Beeler et al., 2008]. A detailed discussion of the first weakening we observed in our experiments will be the focus of a future contribution. For now, we note that the threshold slip velocity for our samples predicted from equation (3) using the properties ( $C_p$ ,  $T_w$  and  $\tau_a$ ) of labradorite, enstatite and diopside (which constitute 80% of the microgabbro, see Table 1), is between 0.07 and 1.6 m/s assuming a typical asperity diameter of 1–10  $\mu\text{m}$ . These velocities are well within the range of velocities in which we observe the first strong weakening (0.05–0.2 m/s), although we must emphasize that the evolution of the interface during initial sliding is probably very complex and dynamic, so that an average asperity size might not be very representative.

[25] Following the initial sharp weakening, a broader strengthening is observed yielding to a second peak (point c in Figure 5a). This broad strengthening has been previously ascribed to (1) the development and linkage of extremely thin, highly discontinuous and viscous melt patches along the sliding surface (experiments on gabbro) [Hirose and Shimamoto, 2005a] or (2) the formation of a highly viscous non-Newtonian rheology layer due to local formation of melt (100 nm in thickness or less) in a grain supported matrix (experiments on peridotite) [Del Gaudio et al., 2009]. After the second peak in friction, friction drops drastically, approximately following an exponential decay with sliding distance until a steady state value is reached. The exponential decay toward a steady state value has been related to the progressive thickening of the throughgoing melt layer, lowering the effective strain rate and thus shear stress until a steady state between melt production and melt extrusion is reached and temperature and melt layer thickness remain constant [Hirose and Shimamoto, 2005a; Nielsen et al., 2008]. This interpretation is supported by movies acquired with an infrared high-speed camera (acquisition rate 1 to 0.1 kHz), which show that the exponential decay occurs when a continuous melt layer is clearly visible. Although we have no direct experimental evidence that this is indeed the mechanism of weakening (experiments were not stopped and samples not collected during the strengthening and the transient; i.e., points b–d in Figure 5b), the data support the model of weakening proposed by Nielsen et al. [2010a] which shows that the duration and the shape of the observed weakening transient are compatible with the formation, by heat diffusion, of a thermal boundary layer in the solid rock on both sides of the melt layer, usually larger (of the order of 1 to a few mm) than the melt layer itself (a fraction of mm). Finally, at the end of the experiment we observe a sharp increase in strength when the sample is decelerating. The increase in friction is strongly related to the deceleration and can potentially be ascribed to an increase in viscosity of the melt layer and a

thinning of the melt layer owing to the lower heat production and melt temperature decrease. The progressive increase of strength can principally be related to the decrease of slip rate, while the final measured shear stress depends on the torque exerted by the machine at the moment of full stop of rotation. In previous data, the absence of a braking mechanism implied that the restrengthening curve was related to inertial effects of the apparatus [Del Gaudio et al., 2009]. We will discuss the restrengthening behavior in more detail in a separate contribution.

## 6.2. Normal Stress Dependence of Steady State Shear Stress

[26] We presented the results of all our experiments in terms of a friction coefficient (shear stress divided by normal stress). However, contrary to the case of solid friction where the friction coefficient is almost independent of normal stress (Amonton's law), we have demonstrated that the friction coefficient at steady state is strongly dependent on the applied normal stress (Figure 6b). This is typical of fluid-lubricated systems [Persson, 2000] and thus the friction coefficient might not be a useful parameter to investigate fault strength in the presence of friction melts [Di Toro et al., 2006b]. In Figure 11, we show the shear stress at the onset of bulk melting (i.e.,  $\tau_p$  or the shear stress at point c in Figure 5a) and the shear stress at steady state ( $\tau_{ss}$  or the average shear stress from points d to e in Figure 5a) as a function of the applied normal stress for all experiments conducted at a sliding velocity of 3 m/s for the steady state and at an acceleration of 30 m/s<sup>2</sup> for the peak. Both the peak and the steady state shear stress increase with normal stress in a strongly nonlinear fashion. Nielsen et al. [2008] derived a steady state traction expression for a melt-lubricated fault as to a power law in the form:

$$\tau_{ss} = C(\sigma_n - \sigma_0)^p \quad (4)$$

where  $C$  is a factor including the velocity dependence and a number of rock, melt and geometrical parameters and  $\sigma_0$  is a finite normal stress or “the residual normal stress” (interpreted by Nielsen et al. [2010b] in terms of partial solid-solid contacts through asperities across the melt layer) and  $p$  is an exponent smaller than 1 (Nielsen et al. [2008] proposed  $p = 1/4$  on the basis of theoretical arguments). Here we propose to fit the experimental data with a power law in the form of equation (4), for both the steady state and the peak shear stress (although we provide no theoretical explanation for the peak value, we attempt an empirical fit). If we fix the exponent to  $p = 1/4$ , however, we are forced (in order to obtain a reasonable fit) to add an extra term to equation (4) such that

$$\tau_{ss} = C_1 + C(\sigma_n - \sigma_0)^{1/4} \quad (5)$$

with values of 5.22 MPa<sup>3/4</sup>, −5.62 MPa and −2.01 MPa for  $C$ ,  $C_1$ , and  $\sigma_0$  for the peak and 1.89 MPa<sup>3/4</sup>, −1.93 MPa and −1.80 MPa for the steady state case. Although the fits are good (as evidenced by  $R^2$  values of 0.94 and 0.98 for peak and steady state, respectively), we rather discard the form of equation (5) because it requires a negative residual stress, which is an unphysical feature (we do not expect suction to develop, or else our vision of the dynamics in the melt layer should be revised to include unknown and severe turbulence

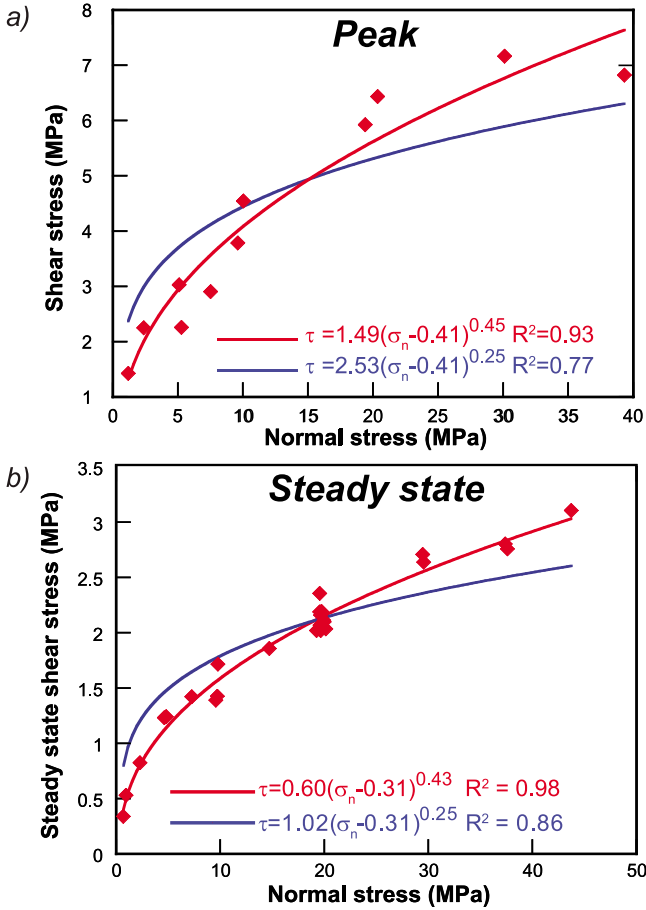


**Figure 11.** (a) Plot of the shear stress at the onset of bulk melting (“peak”) determined using equation (3) as a function of normal stress. Note that only data with an acceleration of  $30 \text{ m/s}^2$  are shown here. Empirical fits using a power law equation with a free exponent and a fixed exponent of 0.25 are also shown. (b) Plot of the steady state shear stress as a function of normal stress. Empirical fits using a power law equation with a free exponent and a fixed exponent of 0.25 are also shown.

effects). The additional term  $C_1$ , however, would be reasonable because a viscous layer would oppose shear even under virtually zero normal stress. Finally, the overall fit obtained with equation (5) is clearly less compatible than a simpler fit obtained by modifying the exponent. In alternative, using equation (4) we may modify the value of exponent  $p$ , obtaining values of  $1.49 \text{ MPa}^{(0.55)}$ ,  $0.41 \text{ MPa}$  and  $0.45$  for  $C$ ,  $\sigma_0$  and the exponent for the peak and  $0.60 \text{ MPa}^{(0.57)}$ ,  $0.30 \text{ MPa}$  and  $0.43$  for the steady state. This strongly suggests an exponent value  $p = 1/2$  which, indeed, provides a fit practically as good as  $p = 0.43–0.45$ . We do not yet have a clear explanation of the discrepancy between the theoretical model and our data. In deriving their equation for the dependence of shear stress on normal stress, Nielsen et al. [2008] assume that shear stress results from the shear of the viscous melt layer, whose properties (e.g., thickness, temperature, equivalent viscosity) result from a system of four equations. One of these equations relates the melt extrusion rate to the normal stress and melt thickness assuming that

the extrusion flow can be approximated as a laminar flow between two parallel disks or rings. The latter approximation is quite strong given that the melt layer thickness is highly variable, and that many asperities practically touch each other across the melt layer [Nielsen et al., 2010b]. Hence, we surmise that the discrepancy between the observed and predicted exponents in the steady state behavior may originate in the simplistic description of the extrusion mechanism. Former experimental data covered a limited range of normal stresses and it was thus not possible to distinguish the predicted  $1/4$  exponent in favor of one closer to  $1/2$ . Alternatively, it is possible that the shear stress is not fully supported by viscous shear, but some more complicated combination of solid and viscous shear is occurring.

[27] According to Nielsen et al. [2010b], the residual normal stress  $\sigma_0$  results from a partial contact through asperities across the melt. A small portion of the normal load is supported by these contacts, the rest is supported by the pressure of the viscous melt layer. In comparison, Nielsen et al. [2008] found a value of  $1.2 \text{ MPa}$  for  $\sigma_0$  for the steady state in gabbro, but using an exponent of  $0.25$ . Our value of  $0.3 \text{ MPa}$  is slightly lower than this estimate, which could be the result of using a different exponent. An alternative explanation is that in our higher-power experiments (sliding velocity of  $3 \text{ m/s}$  and normal stress up to  $40 \text{ MPa}$ , as compared to  $1 \text{ m/s}$  and  $\sim 20 \text{ MPa}$  in the work of Nielsen et al. [2008]), a smaller portion of the normal load is supported by solid-solid contacts. Interestingly, the residual normal stress decreases from the peak to the steady state ( $0.41$  to  $0.3 \text{ MPa}$ ), which seems to suggest that the amount of solid-solid contacts on the sliding interface evolves during the exponential weakening toward steady state. At the same time, the dependence on normal stress (i.e., the power exponent) is roughly the same for the peak and the steady state. We may assume that this similar power law dependence of the peak stress on normal stress has a common origin, although its theoretical counterpart has not yet been investigated.

### 6.3. Slip-Weakening Distance

[28] Previous experimental studies [e.g., Hirose and Shimamoto, 2005a, 2005b; Del Gaudio et al., 2009] observed that the melt-induced weakening (points c and d in Figure 5a, so after the peak in friction coefficient,  $\mu_p$ ) roughly follows an exponential decay with displacement and thus inverted their data with the following equation:

$$\mu = \mu_{ss} + (\mu_p - \mu_{ss}) \exp \left[ \ln(0.05) \frac{d - d_p}{d_w} \right] \quad (6)$$

where  $\mu_{ss}$  is steady state friction,  $d_p$  is displacement at the peak (point c in Figure 5a) and  $d_w$  is the distance required for friction to drop to 95% of the difference between peak and steady state friction.  $d_w$  is usually denoted  $d_c$  in other high-velocity experiment studies but, to avoid confusion with the characteristic or critical slip distance used in rate and state friction modeling, we choose to use  $d_w$  (as in the work of Niemeijer et al. [2010]). We fitted our data using equation (4) with a fixed displacement at the onset of weakening (corresponding to the distance from 0 to point c in Figure 5b) and with all other parameters free. We also obtained the slip-weakening distance by simply measuring it directly from the

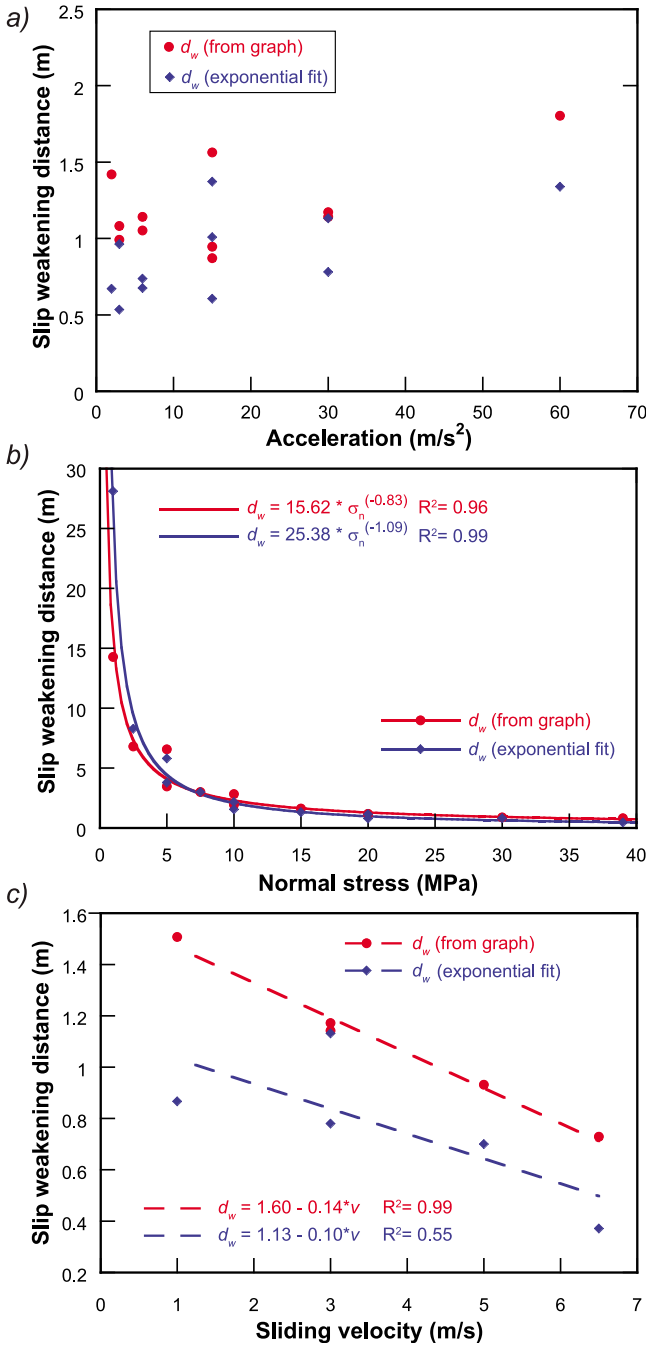


**Figure 12.** Plots of the slip-weakening distance  $d_w$  for the three investigated variables: (a) as a function of acceleration, (b) as a function of normal stress (the data can be fit quite well with a power law equation), and (c) as a function of slip velocity (the data seems to indicate a roughly linear decrease in slip-weakening distance).

graph. Both distances are shown in Figure 12 as a function of acceleration, normal stress and slip velocity. There is significant scatter in the data for the experiments performed with different accelerations and there does not appear to be a strong dependence of the slip-weakening distance on the imposed acceleration, although there is a tendency for the distance to become longer with increasing acceleration (Figure 12a). A

linear fit through the data yielded an  $R^2$  value of only 0.38, so the fit is not significant. Moreover, it is rather surprising that the slip-weakening distance should increase with increasing acceleration, since an increased acceleration would increase the heat rate produced from sliding. However, the initial shear stress is also lower with increasing acceleration (Figure 7a), so this would lower the heat production rate. Since the heat production rate is the product of shear stress and velocity, it is possible that the increase in sliding velocity associated with increasing acceleration is more or less balanced by the decrease in shear stress, so that the heat production rate is constant while acceleration varies. Since the slip-weakening distance is related to the reduction in viscosity of the molten layer owing to an increase in thickness of the molten layer and an increase in temperature, it should not vary with acceleration if the heat production rate remains constant.

[29] In contrast, we observe a strong dependence of the slip-weakening distance on the applied normal stress (Figure 12b). Increasing normal stress results in increased shear stress and thus the heat production rate increases and the slip-weakening distance shortens. The slip-weakening distance decreases with normal stress almost perfectly as  $1/\sigma_n$  (power exponent is between  $-0.83$  and  $1.09$ , depending on the method used to measure the slip-weakening distance). In addition to the normal stress dependence, the slip-weakening distance shows a mild dependence on the sliding velocity (Figure 12c). The data can be fit with a linear equation with a slope of  $0.1$  (for the exponentially fitted  $d_w$ ) and  $0.14$  (for  $d_w$  obtained from graphical inspection). A possible explanation of the  $1/\sigma_n$  and velocity dependence is given below.

[30] We assume that the observed slip weakening is completed when a continuous low-viscosity film of melt has grown to a finite thickness across the slipping zone, which occurs when the temperature reaches or surpasses a given threshold throughout a finite thickness of material [Fialko and Khazan, 2005; Hirose and Shimamoto, 2005a; Del Gaudio et al., 2009]. If temperature is a key control parameter, we know that a frictional heat source of constant power  $\tau V$  imposed at the slipping surface results in a temperature increase such that  $\Delta T \propto \tau V \sqrt{t}$  [Carlslaw and Jaeger, 1959], thus the time necessary to reach a certain temperature threshold scales as  $t \propto (\tau V)^{-2}$  [Beeler et al., 2008; Brantut et al., 2008; Nielsen et al., 2008]. Slip increases linearly in time under constant velocity so that we can write  $t = d_w/V$  and obtain that the slip-weakening distance should scale as  $(\tau V)^{-2}$ . However,  $\tau V$  is not constant during initial sliding, because shear stress scales with  $\sigma_n$  in some complex manner, so that temperature rise cannot be characterized unequivocally. For experiments with relatively low heat production ( $1 < \tau V < 50 \text{ MW/m}^2$ ), the premelting phase lasts for up to several seconds and dominates the weakening interval. Assuming that shear stress in such time interval is roughly constant and proportional to normal stress, the average heat production rate can be approximate by  $\mu \sigma_n V$  (i.e., Mohr-Coulomb type friction); the time to reach a threshold temperature then scales as  $(\sigma_n V)^{-a}$  and the slip-weakening distance scales as  $(\sigma_n V)^{-a}$ , where  $a = 2$ . With increasing power ( $\tau V$ ), the premelt phase becomes less dominant and the dependence of the slip-weakening distance on  $\sigma_n$  and  $V$  changes, through the changing dependence of  $\tau$  on  $\sigma_n$ ; no simple theoretical argument can be made but according to

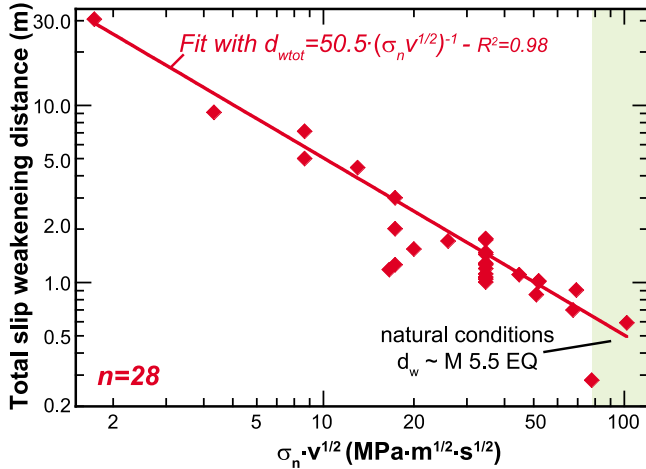


**Figure 13.** Log-log plot of all available total slip-weakening distances (i.e., from all experiments presented here) as a function of  $\sigma_n \sqrt{V}$ , a measure of the power output applied to the samples. Note that our experiments at the highest normal stress and sliding velocity combinations approach the power expected in the upper part of the crust (i.e., at a slip velocity of 1 m/s; normal stress is 100 MPa, equivalent to ~4 km depth for a dry normal fault and to ~6.5 km for a normal fault at hydrostatic pressure). Note that the measured slip-weakening distance under these conditions equates to an earthquake of magnitude 5.5.

Nielsen et al. [2010a] an empirical fit of previous experimental data for  $d_w$  in the presence of melt is compatible with a power law in  $(\sigma_n \sqrt{V})^{-a}$ , where  $a$  is on average close to 1.

[31] In our experiments, we observed an exponential dependence of  $\tau$  on  $\sigma_n$  with an exponent of ~0.5 for both peak (start of weakening) and steady state (end of weakening) shear stress, which, following the thermal arguments of the above paragraph, would explain an exponent  $a = 1$ . Our experiments have a heat production of ~10–120 MW/m<sup>2</sup> and given that this range is rather extensive, we can assess whether the theoretical power law fits well with our data. While the traction evolution is complex and the definition of two distances ( $d_p$  and  $d_w$ ) is necessary to capture its detail, it is the total weakening distance ( $d_p + d_w$ ) which is the most relevant parameter for purposes of source modeling, seismology and the energy balance of fracture propagation. Therefore, in the following we show the total slip-weakening distance ( $d_p + d_w$ ) of all experiments as a function of  $\sigma_n \sqrt{V}$  (Figure 13). The fit to the data represents a power law with the exponent set to 1, for which we obtain a goodness of fit of 0.978 ( $R^2$  value). A power law fit where the exponent is not set, leads to an exponent of -1.102, with the  $R^2$  value increasing slightly to 0.984. We emphasize that the slip-weakening distance appears to be controlled by the power ( $\tau V$ ) applied to the sample. If either of our empirical relations holds, extrapolating the slip-weakening distance to seismicogenic conditions in terms of normal stress and slip velocity would yield  $d_w$  in the order of several centimeters to decimeters. Note that the power values as represented by  $\sigma_n \sqrt{V}$  for the high end of our experimental range are compatible with earthquakes on dry normal faults at a depth of ~4 km, assuming a seismic slip velocity of 1 m/s (i.e., a normal stress of 100 MPa). The slip-weakening distance as determined by

our experiments under these conditions would be equivalent to an earthquake of magnitude ~5 to 5.5.

## 7. Comparison With Natural Fault Zones

[32] Several authors have used the occurrence and characteristics of pseudotachylites to infer the deformation conditions during their formation [Sibson, 1975; Wenk et al., 2000; Hirose and Shimamoto, 2005b; Di Toro et al., 2006b; Andersen et al., 2008; Nielsen et al., 2010b]. Assuming that all heat produced during sliding goes into melting of the fault rock (the process is adiabatic and there is no time for heat to diffuse in the wall rocks) [e.g., Sibson, 1975; Di Toro et al., 2005, 2006b; Hirose and Shimamoto, 2005b] and that the pseudotachylite is formed in a single event (or that the energy dissipated to produce new surfaces is negligible compared to the energy dissipated as frictional heat: there is some evidence for this in the case of pseudotachylites) [Pittarello et al., 2008], the average shear stress (so the shear stress during slip, independently of the presence of a steady state) during seismic slip can be estimated using [Sibson, 1975; Di Toro et al., 2005; Wenk et al., 2000]:

$$\tau_{av} = \rho \cdot E \cdot t/d = \rho t [(1 - \phi)H + C_p \Delta T]/d \quad (7)$$

where  $\rho$  is the rock density,  $E$  is the energy required to heat and melt 1 kg of rock,  $t$  is the pseudotachylite thickness and  $d$  is the seismic slip that produced the pseudotachylite,  $\phi$  the clast fraction with respect to the total volume of the pseudotachylite,  $H$  the latent heat of fusion,  $C_p$  the specific heat at constant pressure and  $\Delta T$  the temperature increase from ambient temperature to melting temperature. From Figure 10, we might estimate a clast fraction  $\phi$  of 0.3. According to the mineral composition reported in Table 1, for the studied microgabbro we might expect  $\rho = 3037 \text{ kg m}^{-3}$ ,  $H = 344.38 \text{ MJ/kg}$ ,  $C_p = 1167 \text{ J kg}^{-1} \text{ K}^{-1}$  (for a temperature of 850°C) and for a temperature increase  $\Delta T = 1400^\circ\text{C}$  (melting of labradorite, enstatite and diopside, the most abundant minerals in the microgabbro), we obtain that  $E$  is 1.66 MJ/kg. Using our experimental shortening data, we can try to estimate the average shear stress using equation (7), assuming that the amount of shortening is equivalent to the amount of melt produced during the experiment.

[33] Figure 14 shows the comparison of the average shear stress estimated with this method and that measured for two experiments performed at different normal stresses and for all experiments with varying normal stress. It is clear from Figures 14a and 14b that some amount of accumulated displacement is required in order to reliably estimate the shear stress. Moreover, Figures 14a and 14c show that the estimate becomes unreliable when the normal stress is low (<~20 MPa). There are at least three reasons that explain the discrepancy between calculated and measured average shear stresses at low normal stresses:

[34] 1. The temperature increase rate in the slipping zone is low and heat diffuses into the wall rocks: this violates the first assumption of equation (7), since the melting process is not adiabatic. At high normal stress, the increase in temperature in the slipping zone is so fast that basically there is no time for heat to diffuse in the wall rocks, as the melting front moves together with the thermal perturbation and the process is virtually adiabatic.

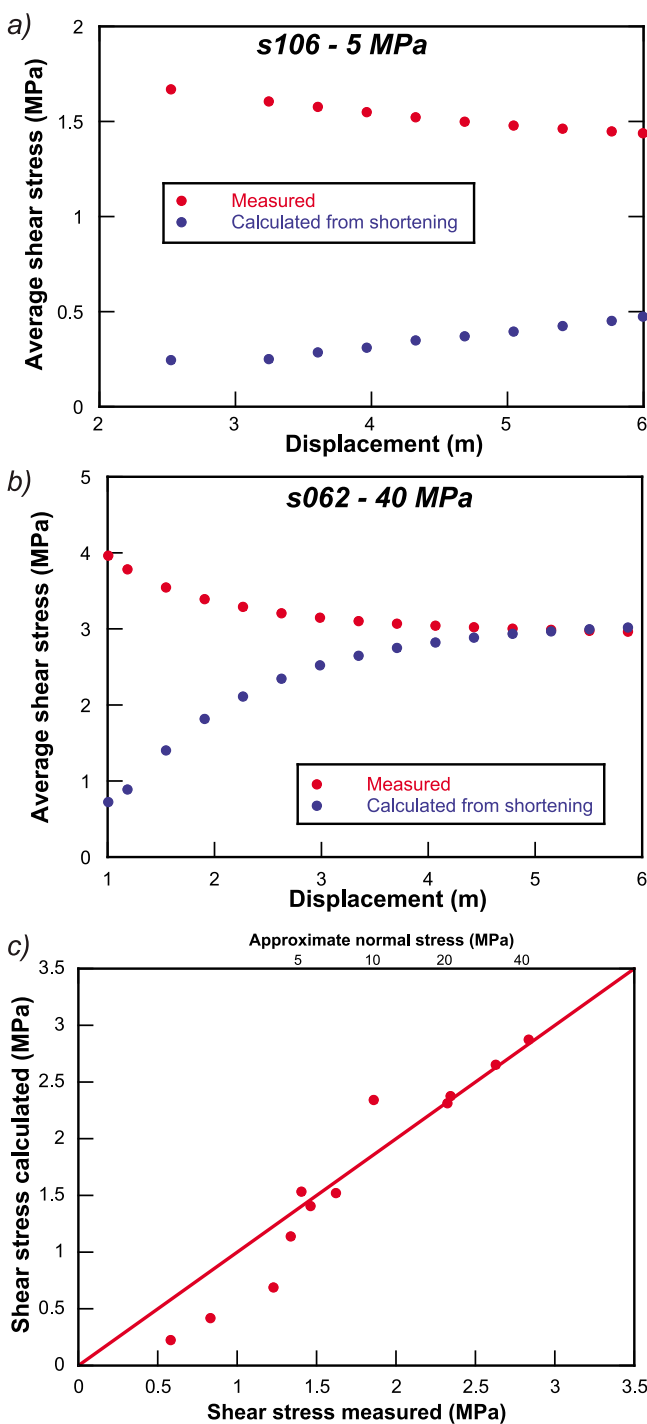


**Figure 14.** Plots of the measured average shear stress and that calculated from the amount of melt produced (i.e., the amount of shortening). (a) Low normal stress experiment (s106). Note that the calculated shear stress is significantly smaller, possibly indicating that not all heat is exchanged to melt the rock. (b) High normal stress experiment (s062). Note that the calculated shear stress overlaps the measured shear stress for displacements  $>4$  m. (c) All experiments with  $30 \text{ m/s}^2$  acceleration and a slip velocity of  $3 \text{ m/s}$ . Average shear stress was calculated at a displacement of 5 m. Note the excellent agreement at higher shear stresses (i.e., high normal stress).

[35] 2. The effect of the initial transient is still dominant (i.e.,  $d_w$  shortens with increasing normal stress; see Figures 12b and 13) which results in a more relevant amount of energy expended in rock comminution: this violates the second main assumption of equation (7) about energy partitioning and alters the estimate of average stress.

[36] 3. Since in low normal stress experiments the complex evolution toward steady state is longer in duration, heat loss to ambient air is in proportion more important for those experiments performed at lower normal stress/velocity (again, this point violates the adiabatic condition assumption of equation (7)). Instead, at higher normal stresses, the heat production is much higher and bulk melting is achieved in a fraction of a second; as a consequence, the two main assumptions of equation (7) (i.e., adiabatic conditions and energy partitioning) are satisfied and the estimate from the amount of shortening compares favorably with the measured shear stress. This confirms that under deformation conditions that approach natural seismic slip, the total amount of shortening is only a function of the heat production (cf. equation (7)) [Sibson, 1975; Di Toro et al., 2005; Wenk et al., 2000] and that shortening rate depends linearly on  $\tau V$  compatibly with the theoretical derivation of Sirono et al. [2006] and Nielsen et al. [2008] and Figure 14c.

[37] In nature, the ambient temperature and normal stress are much higher so that the method of estimating the average shear stress during a single event from the thickness of a pseudotachylite seems to be pretty robust.

[38] The same method of estimating average shear stress has been used on a series of exposed pseudotachylite-bearing faults with varying amounts of separations (which is assumed to correspond roughly to displacement; see, for discussion, Sibson [1975], Di Toro et al. [2006b], and Nielsen et al. [2010a]) from the southern segment of the Outer Hebrides Thrust in Scotland. The data were collected from single jerk faults located in the footwall of the thrust in the Island of North Uist (data in the work of Sibson [1975]) and in the Island of Barra (data collected by T. Hirose and reported in the work of Nielsen et al. [2010a, Table 4]). The pseudotachylites from the southern segment do not have a ductile (equal to crystal-plastic) overprint as the pseudotachylites outcropping in the northern segment [White, 1996] and crosscut a quartz-gneissic gneiss. These microstructural constraints suggest that seismic faulting in the southern segment occurred at ambient temperatures of less than  $280^\circ\text{C}$ , the cataclastic-crystal-plastic transition for quartz which is one of the most important rock-forming minerals of the studied gneiss [e.g., Souquiere, 2010]. Assuming a typical geotherm of  $30^\circ\text{C/km}$ , this temperature corresponds to a depth of less than 10 km. Sibson [1975] estimated the depth of formation of the North Uist pseudotachylites to be between 4 and 10 km. Using the field measurements of separations and thicknesses of several pseudotachylite-bearing fault segments [Sibson, 1975, Tables 3 and 4; Nielsen et al., 2010a], and, for the gneiss,  $E = 1.76 \text{ MJ/kg}$  and  $\rho = 2700 \text{ kg/m}^3$  [Di Toro et al., 2006b], from equation (7), an “average” shear stress-displacement curve was reproduced [Nielsen et al., 2010a]. In this manner, a slip-weakening distance of 0.2–0.4 m was implied for the seismic events that produced the pseudotachylites in the Outer Hebrides Thrust. In the case of frictional melting of silica-built cohesive rocks, the composition of the country rock has little effect on melt lubrication, as

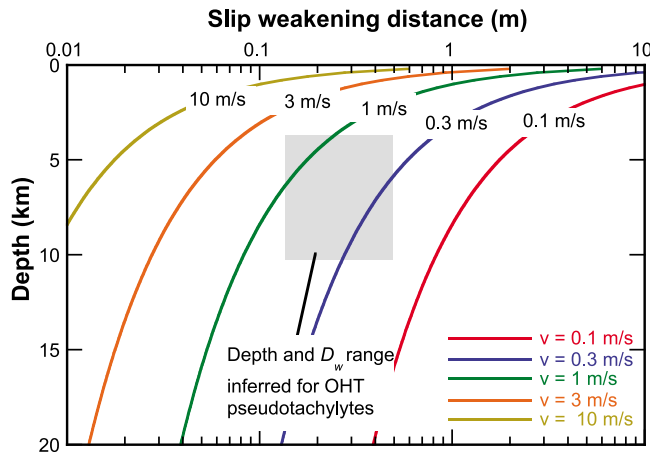


**Figure 15.** Plot of the predicted slip-weakening distance as a function of depth for different slip velocities and thrust fault setting. The curves were calculated using the experimentally determined equations for the normal stress and slip velocity dependence of the slip-weakening distance. Also shown are the depth range and slip-weakening distance inferred for pseudotachylites from the Outer Hebrides Thrust. Note that in this extrapolation we ignore the increase in ambient temperature.

evidenced by experiments performed in rocks having a quite different  $\text{SiO}_2$  content (45% for peridotite, 65% for tonalite and 100% for novaculite) [Di Toro *et al.*, 2006b]. Silica-rich melts are more viscous than silica-poor melts and, as a consequence, are expected to be less lubricant than silica-poor melts [Spray, 1993]. However, the similar lubricating effects, almost independent of the  $\text{SiO}_2$  content, can be interpreted as a feedback effect between temperature and melt viscosity [Sirono *et al.*, 2006]. Depending on the driving forces stored in the wall rocks, an initial high viscosity of the melt induces additional shear heating and higher temperatures, lowering the melt viscosity. Thus, once melt is produced and thermal runaway is achieved, the effect of lubrication on dynamic fault strength is similar for different rocks [Sirono *et al.*, 2006]. Both melting time and duration of weakening once the melt is produced, depend on how fast the temperature rises to melting temperature or slightly above (superheating of the melt), and how fast melt is produced (growth of a minimum layer thickness).  $T_{\text{melt}}$  is not hugely different from one rock to another (at most a factor of two), and neither are the latent heat and heat capacity terms controlling the melt production rate. Therefore, we expect similar evolution of slip-weakening distance in different crystalline rocks, regardless of the silica proportion. This is confirmed by a review of experiments performed at seismic slip rates, where  $d_w$  in the case of friction melting converges to a similar value in different rocks at normal stress of 20 MPa [Di Toro *et al.*, 2011, Figure 2]: we infer that at seismogenic depths (e.g.,  $\sigma_n > 100 \text{ MPa}$ ), the  $d_w$  is comparable for rock types with different compositions. As a consequence, it might be interesting to see how our experimentally determined slip-weakening distance compares with the one estimated from natural faults, even in the case of host rocks with a different composition than our samples.

[39] To do this, we used the empirical equations for the slip velocity (see Figure 12c) and normal stress dependence of the

slip-weakening distance (see Figure 12b) to predict the slip-weakening distance at depth for the Outer Hebrides Thrust. As previously discussed, the faults were exhumed from an estimated depth ranging from 4 to 10 km. For a typical lithostatic stress gradient of 27 MPa/km or an overburden rock density of  $2700 \text{ kg/m}^3$ , the stress normal to the thrust

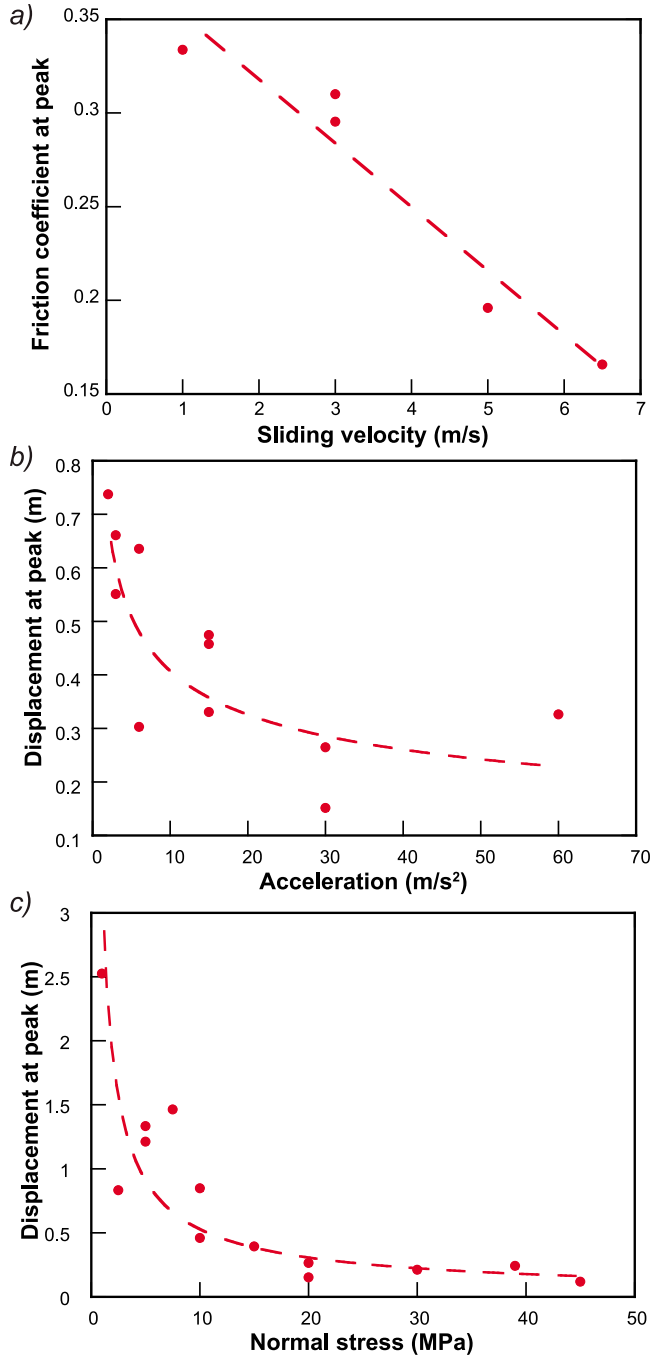


**Figure 16.** (a) Plot of the friction coefficient at the onset of bulk melting (“peak” determined using equation (3)) as a function of sliding velocity. (b) Plot of the displacement at which the peak occurs (determined using equation (3)) as a function of acceleration. (c) Plot of the displacement at which the peak occurs (determined using equation (3)) as a function of normal stress.

fault at the time of seismic faulting ranged between  $200 < \sigma_n < 500$  MPa. Ignoring the effect of increasing ambient temperature, the depth range and slip-weakening distance that are inferred for the production of the Outer Hebrides Thrust pseudotachylytes roughly bound a region of average slip velocities for these events of 0.3 to 1 m/s (Figure 15). This estimate is consistent with average slip velocities from seismic inversion data of actual earthquakes [Heaton, 1990] and with earlier estimates of minimum slip velocities for these pseudotachylytes [Sibson, 1975].

## 8. Threshold Distance and Stress for Melt-Lubricated Weakening

[40] In addition to the dependence of the peak shear stress (point c in Figure 5) on normal stress at the onset of bulk melting (Figure 11a), we also find a dependence of peak shear stress on the slip velocity (Figure 16a). In addition, the slip distance required to reach this peak stress depends strongly on the acceleration and normal stress (Figures 16b and 16c). Taken together, these observations suggest that the production of melt patches that strengthen the fault during the transient stage leading up to the dramatic weakening caused by bulk melting and lubrication might actually arrest a rupture when the effective normal stress is low (high peak stress and long distance) and the acceleration and slip velocity are small (increasing distance to peak stress) [Fialko and Khazan, 2005]. In addition, in natural faults the presence of a fluid (pressure) might lead to thermal pressurization of the fluid during the initiation of rapid slip [Andrews, 2002; Wibberley and Shimamoto, 2005; Bizzarri and Cocco, 2006; Rempel and Rice, 2006], so that the effective normal stress is reduced. If the reduction of normal stress does not inhibit the production of melt, then it would in turn lead to a relative increase in shear stress (i.e., a larger coefficient of friction) which could effectively halt a rupture.

## 9. Conclusions

[41] In this study, we presented results from rock-on-rock sliding experiments on samples of gabbro at high slip velocities, normal stresses and with variable accelerations and decelerations using a newly developed high-velocity rotary shear apparatus (SHIVA). Our results compare well with previous experiments investigating frictional melting, but we extend the range of normal stress up to 45 MPa and use ring-shaped samples providing a more accurate measure of slip velocity and shear stress. Moreover, we systematically varied the imposed acceleration and deceleration to investigate their effect on the evolution of shear stress. We reached the following conclusions:

[42] 1. Variable acceleration does not affect the steady state shear stress in the melt-lubricated regime, but affects the initial shear stress evolution.

[43] 2. Increasing normal stress leads to a mild increase in shear stress, demonstrating a clear deviation from a Mohr-Coulomb-type linear relation. Instead, we found that steady state shear stress increases with normal stress according to a power law with a stress exponent of 0.5, in contrast to theoretical models of melt lubrication [Nielsen et al., 2008].

[44] 3. Comparison of average shear stress estimated via the amount of shortening (i.e., melt produced) with the

measured shear stress shows that it is plausible to use this method on exhumed pseudotachylytes as long as the normal stress is high ( $>\sim 20$  MPa).

[45] 4. The slip-weakening distance is not a scale-independent variable, but depends systematically on normal stress and slip velocity.

[46] 5. Extrapolation of the empirically determined relations between slip-weakening distance, normal stress and slip velocity to the formation conditions of the pseudotachylytes of the Outer Hebrides Thrust suggests that these were formed at slip velocities of 0.3 to 1 m/s.

[47] 6. At small normal stress (in the shallow crust) the presence of a threshold in shear stress due to the formation of discontinuous highly viscous patches of melt inhibits the lubricating effects of friction melting.

[48] 7. Experiments that reproduce the combination of normal stress and slip rates achieved in actual earthquakes suggest that the slip-weakening distance might be in the order of few tens of centimeters at most, suggesting that melt lubrication might be activated in moderate to large size earthquakes.

[49] **Acknowledgments.** A.N., G.D.T., and S.N. designed the experimental study and contributed to the manuscript, A.N. ran the experiments, and A.N. and F.D.F. improved SHIVA. The authors wish to thank Hiroki Sone and Associate Editor John Spray for their thoughtful and constructive reviews. The authors thank Giovanni Romeo and Massimo Mari for designing and building the in-house-built encoder; Piergiorgio Scarlato for encouraging this work and helping in the installation of SHIVA; Elena Spagnuolo and Gianni Romeo for working on the vibration issue; Tom Mitchell, Steve Smith, and Terry Tullis for help and suggestions that helped improve the initial experiments; Giuseppe Di Stefano for designing the original data acquisition system; Takehiro Hirose for running the experimental comparison with identical gabbro; and the engineers and technicians from the machine shop at Realizzazione Meccanica e Progettazione, Acilia, Rome, for building and troubleshooting the apparatus. This research was funded by the European Research Council Starting Grant Project 205175 (USEMS). A.N. was funded in part by VENI grant 863.09.013 of the Netherlands Organisation for Scientific Research.

## References

- Abercrombie, R., A. McGarr, G. Di Toro, and H. Kanamori (Eds.) (2006), *Earthquakes: Radiated Energy and the Physics of Faulting*, *Geophys. Monogr. Ser.*, vol. 170, 327 pp., AGU, Washington, D. C.
- Andersen, T. B., K. Mair, H. Austrheim, Y. Y. Podladchikov, and J. C. Vrijmoed (2008), Stress release in exhumed intermediate and deep earthquakes determined from ultramafic pseudotachylite, *Geology*, **36**, 995–998, doi:10.1130/G25230A.1.
- Andrews, D. J. (2002), A fault constitutive relation accounting for thermal pressurization of pore fluid, *J. Geophys. Res.*, **107**(B12), 2363, doi:10.1029/2002JB001942.
- Beeler, N. M., T. E. Tullis, and D. L. Goldsby (2008), Constitutive relationships and physical basis of fault strength due to flash heating, *J. Geophys. Res.*, **113**, B01401, doi:10.1029/2007JB004988.
- Bizzarri, A., and M. Cocco (2006), A thermal pressurization model for the spontaneous dynamic rupture propagation on a three-dimensional fault: I. Methodological approach, *J. Geophys. Res.*, **111**, B05303, doi:10.1029/2005JB003862.
- Brantut, N., A. Schubnel, J.-N. Rouzaud, F. Brunet, and T. Shimamoto (2008), High-velocity frictional properties of a clay-bearing fault gouge and implications for earthquake mechanics, *J. Geophys. Res.*, **113**, B10401, doi:10.1029/2007JB005551.
- Byerlee, J. (1978), Friction of rocks, *Pure Appl. Geophys.*, **116**, 615–626, doi:10.1007/BF00876528.
- Carlslaw, H. S., and J. C. Jaeger (1959), *Conduction of Heat in Solids*, Oxford Univ. Press, New York.
- Del Gaudio, P., G. Di Toro, R. Han, T. Hirose, S. Nielsen, T. Shimamoto, and A. Cavallo (2009), Frictional melting of peridotite and seismic slip, *J. Geophys. Res.*, **114**, B06306, doi:10.1029/2008JB005990.
- Di Toro, G., G. Pennacchioni, and G. Teza (2005), Can pseudotachylytes be used to infer earthquake source parameters? An example of limitations

- in the study of exhumed faults, *Tectonophysics*, **402**, 3–20, doi:10.1016/j.tecto.2004.10.014.
- Di Toro, G., T. Hirose, S. Nielsen, G. Pennacchioni, and T. Shimamoto (2006a), Natural and experimental evidence of melt lubrication of faults during earthquakes, *Science*, **311**, 647–649, doi:10.1126/science.1121012.
- Di Toro, G., T. Hirose, S. Nielsen, and T. Shimamoto (2006b), Relating high-velocity rock friction experiments to coseismic slip, in *Earthquakes: Radiated Energy and the Physics of Faulting*, *Geophys. Monogr. Ser.*, vol. 170, edited by R. Abercrombie et al., pp. 121–134, AGU, Washington, D. C.
- Di Toro, G., G. Pennacchioni, and S. Nielsen (2009), Pseudotachylites and earthquake source mechanics, in *International Geophysics*, edited by E. Fukuyama, pp. 87–133, Academic, San Diego, Calif.
- Di Toro, G., et al. (2010), From field geology to earthquake simulation: A new state-of-the-art tool to investigate rock friction during the seismic cycle (SHIVA), *Rend. Lincei*, **21**, suppl. 1, 95–114.
- Di Toro, G., R. Han, T. Hirose, N. De Paola, S. Nielsen, K. Mizoguchi, F. Ferri, M. Cocco, and T. Shimamoto (2011), Fault lubrication during earthquakes, *Nature*, **471**, 494–498.
- Fialko, Y., and Y. Khazan (2005), Fusion by earthquake fault friction: Stick or slip?, *J. Geophys. Res.*, **110**, B12407, doi:10.1029/2005JB003869.
- Goldsby, D. L., and T. E. Tullis (2002), Low frictional strength of quartz rocks at subseismic slip rates, *Geophys. Res. Lett.*, **29**(17), 1844, doi:10.1029/2002GL015240.
- Heaton, T. H. (1990), Evidence for and implications of self-healing pulses of slip in earthquake rupture, *Phys. Earth Planet. Inter.*, **64**, 1–20, doi:10.1016/0031-9201(90)9002-F.
- Hirose, T., and T. Shimamoto (2005a), Growth of molten zone as a mechanism of slip weakening of simulated faults in gabbro during frictional melting, *J. Geophys. Res.*, **110**, B05202, doi:10.1029/2004JB003207.
- Hirose, T., and T. Shimamoto (2005b), Slip-weakening distance of faults during frictional melting as inferred from experimental and natural pseudotachylites, *Bull. Seismol. Soc. Am.*, **95**, 1666–1673, doi:10.1785/0120040131.
- Jeffreys, H. (1942), On the mechanics of faulting, *Geol. Mag.*, **79**, 291–295, doi:10.1017/S0016756800076019.
- Kanamori, H., and T. H. Heaton (2000), Microscopic and macroscopic physics of earthquakes, in *Gecomplexity and the Physics of Earthquakes*, *Geophys. Monogr. Ser.*, vol. 120, edited by J. Rundle, D. L. Turcotte, and W. Klein, pp. 147–163, AGU, Washington, D. C.
- Kanamori, H., and L. Rivera (2006), Energy partitioning during an earthquake, in *Earthquakes: Radiated Energy and the Physics of Faulting*, *Geophys. Monogr. Ser.*, vol. 170, edited by R. Abercrombie et al., pp. 3–13, AGU, Washington, D. C.
- Lee, W. H., H. Kanamori, P. C. Jennings, and C. Kisslinger (2002), *International Handbook of Earthquake and Engineering Seismology*, 933 pp., Academic, Amsterdam.
- McKenzie, D., and J. N. Brune (1972), Melting on fault planes during large earthquakes, *Geophys. J. R. Astron. Soc.*, **29**, 65–78.
- Mizoguchi, K., and E. Fukuyama (2010), Laboratory measurements of rock friction at subseismic slip velocities, *Int. J. Rock Mech. Min. Sci.*, **47**, 1363–1371, doi:10.1016/j.ijrmms.2010.08.013.
- Nielsen, S., G. Di Toro, T. Hirose, and T. Shimamoto (2008), Frictional melt and seismic slip, *J. Geophys. Res.*, **113**, B01308, doi:10.1029/2007JB005122.
- Nielsen, S., P. Mosca, G. Giberti, G. Di Toro, T. Hirose, and T. Shimamoto (2010a), On the transient behavior of frictional melt during seismic slip, *J. Geophys. Res.*, **115**, B10301, doi:10.1029/2009JB007020.
- Nielsen, S., G. Di Toro, and W. A. Griffith (2010b), Friction and roughness of a melting rock interface, *Geophys. J. Int.*, **182**, 299–310.
- Niemeijer, A., C. Marone, and D. Elsworth (2010), Frictional strength and strain weakening in simulated fault gouge: Competition between geometrical weakening and chemical strengthening, *J. Geophys. Res.*, **115**, B10207, doi:10.1029/2009JB000838.
- Persson, B. N. J. (2000), *Sliding Friction*, 515 pp., Springer, Berlin.
- Pittarello, L., G. Di Toro, A. Bizzarri, G. Pennacchioni, J. Hadizadeh, and M. Cocco (2008), Energy partitioning during seismic slip in pseudotachylite-bearing faults (Gole Larghe Fault, Adamello, Italy), *Earth Planet. Sci. Lett.*, **269**, 131–139, doi:10.1016/j.epsl.2008.01.052.
- Reches, Z. E., and D. A. Lockner (2010), Fault weakening and earthquake instability by powder lubrication, *Nature*, **467**, 452–455, doi:10.1038/nature09348.
- Rempel, A. W., and J. R. Rice (2006), Thermal pressurization and onset of melting in fault zones, *J. Geophys. Res.*, **111**, B09314, doi:10.1029/2006JB004314.
- Rice, J. R. (1999), Flash heating at asperity contacts and rate-dependent friction, *Eos Trans. AGU*, **80**(46), Fall Meet. Suppl., F681.
- Rice, J. R. (2006), Heating and weakening of faults during earthquake slip, *J. Geophys. Res.*, **111**, B05311, doi:10.1029/2005JB004006.
- Scholz, C. H. (2002), *The Mechanics of Earthquakes and Faulting*, 2nd ed., 471 pp., Cambridge Univ. Press, Cambridge, U. K.
- Shimamoto, T., and A. Tsutsumi (1994), A new rotary-shear high-speed friction testing machine its basic design and scope of research (in Japanese with English abstract), *J. Tecton. Res. Group Jpn.*, **39**, 65–78.
- Sibson, R. H. (1975), Generation of pseudotachylite by ancient seismic faulting, *Geophys. J. R. Astron. Soc.*, **43**, 775–794.
- Sibson, R. H., and V. G. Toy (2006), The habitat of fault-generated pseudotachylite: Presence vs. absence of friction-melt, in *Earthquakes: Radiated Energy and the Physics of Faulting*, *Geophys. Monogr. Ser.*, vol. 170, edited by R. Abercrombie et al., pp. 153–166, AGU, Washington, D. C.
- Sirono, S., K. Satomi, and S. Watanabe (2006), Numerical simulations of frictional melting: Small dependence of shear stress drop on viscosity parameters, *J. Geophys. Res.*, **111**, B06309, doi:10.1029/2005JB003858.
- Souquière, F. (2010), Mechanics of earthquakes in the continental crust: Insight from the structural analysis of pseudotachylites and cataclasites, Ph.D. thesis, 193 pp., Univ. de Franche-Comté, Besançon, France.
- Spray, J. G. (1987), Artificial generation of pseudotachylite using friction welding apparatus: Simulation of melting on a fault plane, *J. Struct. Geol.*, **9**, 49–60, doi:10.1016/0191-8141(87)90043-5.
- Spray, J. G. (1993), Viscosity determinations of some frictionally generated silicate melts: Implications for fault zone rheology at high strain rates, *J. Geophys. Res.*, **98**, 8053–8068, doi:10.1029/93JB00020.
- Spray, J. G. (2005), Evidence for melt lubrication during large earthquakes, *Geophys. Res. Lett.*, **32**, L07301, doi:10.1029/2004GL022293.
- Tsutsumi, A., and T. Shimamoto (1997), High-velocity frictional properties of gabbro, *Geophys. Res. Lett.*, **24**, 699–702, doi:10.1029/97GL00503.
- Wenk, H. R., L. R. Johnson, and L. Ratschbacher (2000), Pseudotachylites in the eastern peninsular ranges of California, *Tectonophysics*, **321**, 253–277, doi:10.1016/S0040-1951(00)0064-0.
- White, J. C. (1996), Transient discontinuities revisited: Pseudotachylite, plastic instability and the influence of low pore fluid pressure on deformation processes in the mid-crust, *J. Struct. Geol.*, **18**, 1471–1477, doi:10.1016/S0191-8141(96)00059-4.
- Wibberley, C. A. J., and T. Shimamoto (2005), Earthquake slip weakening and asperities explained by thermal pressurization, *Nature*, **436**, 689–692, doi:10.1038/nature03901.

F. Di Felice and S. Nielsen, Istituto Nazionale di Geofisica e Vulcanologia, Via di Vigna Murata 605, I-00143 Rome, Italy.

G. Di Toro, Dipartimento di Geoscienze, Università degli Studi di Padova, Via Gradenigo 6, I-35131 Padua, Italy.

A. Niemeijer, Faculty of Geosciences, Utrecht University, 3584 CS Utrecht, Netherlands. (niemeijer@geo.uu.nl)